# 1

# Oxygen Reduction Reaction Electrocatalysts

*Xinwen Peng and Lei Zhang*

*South China University of Technology, School of Light Industry and Engineering, State Key Laboratory of Pulp and Paper Engineering, Wushan Street, Guangzhou, 510641, P.R. China*

## 1.1 Introduction

With the series of energy crises and environmental pollution by the transition consumption of fossil fuels, the pursuit of new clean alternative sources of energy is becoming more and more urgent [1]. Oxygen reduction reaction (ORR) as an important electrode reaction for proton exchange membrane fuel cells (PEMFCs) and zinc–air batteries (ZABs) to alleviate the current energy and environmental problems have drawn much attention by the scientist [2]. Compared with traditional fuels, PEMFCs are the device that can directly convert chemical energy into electrical energy through electrochemical reactions, which is not restricted by the Carnot cycle and has high energy conversion efficiency (45–60%) [3–5]. The process of power generation is environment-friendly and emits only water as a byproduct, which is called the green energy conversion technology in the twenty-first century [6, 7]. Additionally, ZABs are considered to be safe, economical, and alternative battery systems due to the high abundance of zinc, mild reactivity, low cost, high theoretical energy density, and incombustibility feature of the aqueous electrolytes [1, 2, 8].

However, ORR is an inert reaction, and the poor reaction kinetics of ORR severely restrict the energy conversion efficiency of PEMFCs and ZABs [9]. At present, Pt-based catalysts (mainly Pt/C) are still the most effective ORR electrocatalysts for PEMFCs and ZABs [10, 11]. So, it is necessary to load larger Pt on the cathode to catalyze slow and speed-limited ORR [12]. But, Pt is expensive and easily poisoned by carbon monoxide and methanol, which seriously restricts the large-scale application of PEMFCs and ZABs [4, 6]. Therefore, emerging low-cost ORR catalyst materials with high electrocatalytic activity as well as strong durability has appeared at the front of current research and progress energies headed for PEMFCs and ZABs [7, 13]. So far, many approaches have been developed to synthesize these catalysts, which can be divided into two diverse approaches. The first approach is reducing the dosage of Pt, such as improving the atom utilization of Pt by alloying

*Photo- and Electro-Catalytic Processes: Water Splitting, $N_2$ Fixing, $CO_2$ Reduction*, First Edition.
Edited by Jianmin Ma.

with low-priced metals such as Co, Fe, Ni, etc. [14], boosting the intrinsic catalytic activity, constructing specific nanostructures with Pt-rich surface, and reducing the nanostructure size of Pt-based electrocatalysts [5, 12, 15]. Another approach is the fabrication of non-noble metal electrocatalysts, such as transition metal (TM)-based catalytic materials (metal carbide, metal nitride, metal oxides, metal sulfide, atomically dispersed metal in carbon materials, alloys, etc.) [2, 10, 13, 16] and metal-free materials (N-, P-, S-, B-doped carbon materials, etc.) [1, 17–19]. Recently, excellent progress has been made in controlling the size, morphology, facets, and composition of transition metal-based and metal-free ORR electrocatalysts [7, 17, 20]. In the past few years, our group had also carried out many works to improve the ORR catalytic activity of biomass-derived carbon-based catalysts. For instance, the proposed top-down approach for the bulk transformation of raw wood to prepare the high-efficiency N-doped 3D ORR catalyst (N/E-HPC-900) with a high density of hierarchical pores [2], as well as the proposed simple and convenient manufacturing strategy for high-performance 3D self-supporting flexible carbon aerogel ORR electrocatalysts (FeP/$Fe_2O_3$@NPCA [N, P-doped rGO/CNF carbon aerogel]) [1].

In this chapter, the recent research progress of ORR electrocatalysts for PEMFCs and ZABs is reviewed in detail. The Pt-based electrocatalyst and the non-noble metal electrocatalyst are two research hotspots of ORR electrocatalysts. For non-noble ORR electrocatalysts, transition metals and metal-free materials are made in-depth analysis and comparison. Additionally, we also reviewed and analyzed the activity and stability of ORR electrocatalytic materials in the discharge reaction of ZABs, along with the perspectives on the proper design of carbon-based materials as ORR electrocatalysts for highly efficient ORR in the acid electrolyte.

## 1.2 Pt-Based ORR Electrocatalysts

Although many other types of highly active electrocatalysts have attracted increasing attention to replace expensive precious metal catalysts, Pt-based nanomaterials are still the main electrocatalysts for commercial applications and are often chosen as the benchmark materials for PEMFCs and ZABs [7]. Pt nanoparticles (NPs) are typically loaded onto support materials with high surface areas to increase their dispersibility and increase catalytic activity [21–23]. However, the commercialization of PEMFCs and ZABs is still limited by the high cost of Pt. In recent decades, to increase the stability and catalytic activity of Pt-based catalysts, two methods have been proposed to be effective in enhancing ORR performance: (i) designing the shape, size, and structure of Pt NPs to maximize their specific activity [24, 25] and (ii) alloying or modifying Pt with non-noble metal iron (Fe), cobalt (Co), nickel (Ni), copper (Cu), manganese (Mn), chromium (Cr), and so on to form alloys or core–shell nanostructures [26, 27].

### 1.2.1 Facet-Controlled Catalysts

Basic research studies of Pt have shown that the high-index plane demonstrates higher activity than the common stable plane [28, 29]. Therefore, controlling Pt nanocrystals bounded by a high-index plane is a promising way for improving the catalytic performance of Pt nanocrystals [30]. Sheng et al. exhibited that the successful synthesis of 2–10 nm high-index facet Pt supported by carbon black or graphene can achieve comparable mass activity to commercial catalysts [31]. Zhang et al. adopted a wet chemical route to synthesize concave cubic Pt NPs enclosed by high-index planes (510), (720), and (830). The Pt concave cube provides the ORR with the advantage of uniform surface structure and large surface area. The mass and surface area activity of the obtained catalyst at 0.9 V (vs. reversible hydrogen electrode [RHE]) were higher than that of the commercial Pt/C catalyst [32]. The ORR activity of uniformly dispersed Pt NPs is related to its size, and its ORR activity is reduced in the size range of 2–7 nm. Recently, the researcher demonstrated that the Pt catalyst loaded on the $LiCoO_2$ thin layer that expands and contracts by 0.01 nm when the electrons move in and out almost doubled the catalytic activity of the Pt when the support material contracted during the charge phase. However, detailed experimental studies have shown that no matter the initial shape, Pt NPs are metastable and gradually evolve into thermodynamic equilibrium round shape with similar activity to ORR. Thus, as the particle age, size, and shape effects decrease, it may even seem that the ORR activity is independent of both particle size and particle shape [12]. Structural regulation is another effective way to achieve high ORR catalytic activity, such as assembling 1D nanostructure Pt into 2D membrane or 3D nanonetwork [33–35]. For instance, Lou and coworkers reported on interconnected 3D-Pt-nanometer assembly catalysts [36]. Compared with 0D Pt NPs, the interconnected three-dimensional Pt-nanoassembly exhibited enhanced stability, high electrochemical surface area, and a higher resistance to migration, aggregation, dissolution, and Ostwald ripening.

## 1.2.2 Multimetallic Nanocrystals

### 1.2.2.1 Pt Alloys

The alloy catalyst not only inherits the remarkable electrocatalytic performance of metal Pt but also generally exhibits superior performance to metal Pt [15, 37]. In past years, many Pt bimetallic and trimetallic nanomaterials have been synthesized, for example, coating Pt on metal NPs, Pt/3d transition metal alloying, and dealloying of binary/ternary nanocatalysts, and have shown remarkable performance in the catalytic ORR [38–40]. While transition metal alloying reduces the content of expensive Pt, it can improve the catalytic activity and stability by optimizing their electronic structure and geometric atomic arrangement [41–43]. These geometric and electronic effects lead to the shift of the energetic center of the Pt-projected d-state, affecting the strength of the surface-adsorbed bonds, and thus leading to changes in the chemical adsorption of reactants, intermediates, and products [44]. Polycrystalline $Pt_3M$ film catalysts (M = Fe, Ni, Co, and Ti) were synthesized by Stamenković and coworkers to investigate the function of 3d metals in the oxygen reduction activity of Pt alloys [45]. The results showed that the nature of the 3d metal played a vital role in the catalytic activity of ORR. The fundamental relationship between oxygen reduction activity and the surface electronic structure (the d-band center)

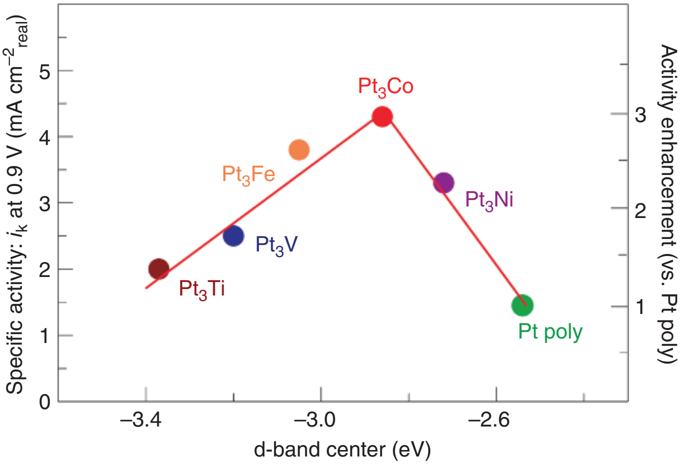

**Figure 1.1** Relationships between experimentally measured specific activity for the ORR on $Pt_3M$ surfaces in 0.1 M $HClO_4$ at 333 K vs. the d-band center position. Source: Reproduced with permission of Stamenković et al. [46], Springer Nature.

for the $Pt_3M$ (M = Co, Ni, Fe, Ti, and V) surfaces is showed in Figure 1.1 [46]. It demonstrated a “volcano-type” relationship in which the optimum catalytic activity is controlled by the balance between the surface coverage of the blocking species and adsorption energy of the reaction intermediate. A better ORR electrocatalyst should have a weaker ability to bind $O_2$ molecules than Pt and enhance the rate of desorption of intermediate products [7, 45]. From this point of view, Co, Ni, and Fe were considered to be most valid alloying elements [45, 46]. Stamenković et al. adopted the solvothermal method to synthesize a series of homogeneous $Pt_3M$ (M = Fe, Co, or Ni) nanocatalysts supported on porous carbon with controllable particle size [14]. Studies on ORR performance showed that the $Pt_3M$ catalysts had enhanced factors of ~2–3 in specific activity vs. Pt at 0.9 V. Compared to $Pt_3Ni$ and $Pt_3Fe$, $Pt_3Co$ had the highest activity. Since the study of single-crystal $Pt_3Ni(111)$ by Stamenković et al., Pt–Ni alloy octahedron has attracted great interest. Recently, the authors optimized the method reported in the literature to synthesize a 9 nm Pt–Ni octahedron having a clear (111) crystal plane on its surface [5]. The Pt/Ni ratio can be controlled in different time ranges under the action of acetic acid at 60 °C, and $Pt_{2.5}Ni$ was 17 times more active at 0.9 V than the Pt/C. The study on the epitaxial surface of $Pt_3Ni(111)$ single crystal showed that the specific activity is 10 times that of the corresponding Pt(111) and 90 times that of commercial Pt/C for the ORR in 0.1 M $HClO_4$ medium [15]. It was found that the three outermost layers of $Pt_3Ni(111)$ were crucial to determine the catalytic properties, in which the third layer was Pt-rich (87% Pt), the intermediate atomic layer is rich in Ni (52% Ni), and the outermost layer contains 100% Pt. Sun et al. prepared monodisperse Pt-M NPs using a simple and yet general approach that co-reduction of $Pt(acac)_2$ and $M(acac)_2$ in the presence of oleylamine at 300 °C (M = Cu, Co, Fe, Ni, Zn) [47]. This versatile approach offers the possibility to investigate in more detail the Pt-based alloy NPs used in ORR catalysis. Recently, a highly durable and active hollow $Pt_3Ni$

nanoframe catalyst with the interior and exterior catalytic surfaces was synthesized [48]. This catalyst with $Pt_3Ni$-/Pt-skin surfaces on high surface area carbon showed a higher specific activity and mass activity for ORR than that of Pt/C. There has been a lot of research studies on the Pt–Co system and has made great progress, including intermetallic Pt–Co nanocatalysts with ordered structure and disordered Pt–Co alloys. For example, Abruña and coworkers successfully prepared Pt–Co NPs with a core–shell structure consisting of an ordered $Pt_3Co$ intermetallic core and a Pt shell with two to three atomic layer [49]. Compared with the disordered $Pt_3Co$–C alloy, $Pt_3Co$@Pt has more excellent activity and durability and has the highest mass activity of Pt.

Porous nanostructure applications have unparalleled advantages in electrocatalysis, such as high specific surface area and low density, while providing sufficient active sites for close-range absorption of molecules. At the same time, this special nanoporosity facilitates the mass transfer of $O_2$ on the metal surface, thereby improving the ORR kinetics by encapsulating $O_2$ on the active metal surface. Therefore, introducing nanoporosity into bimetallic alloys can improve the active surface area and is generally considered to be an available method to increase the catalytic activity [50–52]. Héctor D. Abruña et al. prepared a promising intermetallic NP of $Cu_3Pt$ with low Pt mole fraction [50]. Their results showed a thin Pt skin with a thickness of about 1 nm, and an ordered $Cu_3Pt$ core was obtained by the electrochemical dealloying method, while a "spongy-like" structure without forming an ordered structure was prepared by the chemical leaching. Compared with electrochemically de-alloyed NPs, sponge-like NPs demonstrated lower specific activity and better mass activity after 50 potential cycles [50]. Jonah Erlebacher and coworkers developed a nanoporous Ni/Pt NP catalyst which was made through dealloying of Ni/Pt alloy NPs with rich nickel to study the ORR activity of nanoporous Ni/Pt alloy NPs [53]. It was found that the mass activity of the ORR was almost four times that of the Pt/C, exceeding the comparable nanoporous Pt-skeleton Ni/Pt alloy NPs. Yi Ding and coworkers developed a nanoporous surface alloy structure using a simple two-step dealloying process; the obtained nanostructures are interconnected by ligaments approximately 3 nm in diameter consisting of a Pt/Ni alloy core and an almost pure Pt surface [51]. In their research, they found that these nanoporous surface alloys showed a remarkable specific activity of $1.23\ \mathrm{mA\ cm^{-2}}$ at a high potential (0.9 V vs. RHE) and enhanced durability for ORR [51]. Jiang-Lan Shui et al. prepared Pt–Fe alloy nanowires with nanopores by electrospinning and chemical dealloying techniques [52]. These porous long nanowires with a diameter of about 10–20 nm and the ligament diameter 2–3 nm exhibited a high specific activity. Yadong Li and coworkers developed a facile chemical dealloying strategy to prepare a variety of monodisperse alloy nanoporous NPs using nanocrystalline alloys [54]. The primary electrochemical tests confirmed that alloy nanoporous NPs with small pores and high surface area showed more superior catalytic properties than alloyed NPs. To understand the effect of nanopores on the stability and intrinsic activity of NP electrocatalysts, Peter Strasser and coworkers prepared Pt–Ni bimetallic NPs with a controllable nanopore structure by an atmosphere-controlled acid leaching [55]. Their research showed

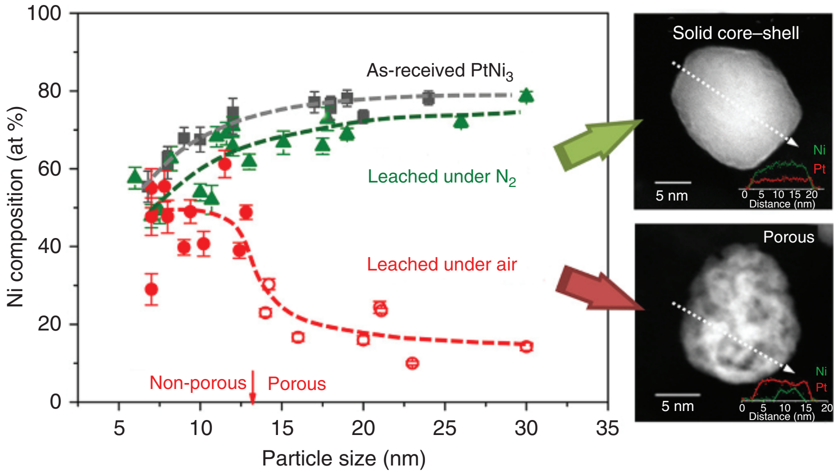

**Figure 1.2** Correlations between particle size, composition, and porosity in the three catalysts (PtNi$_3$, PtNi$_3$ leached under N$_2$, PtNi$_3$ leached under air), where the horizontal dot lines represent the average compositions. Source: Reproduced with permission of Gan et al. [55], American Chemical Society.

that nanoporosity in PtNi NPs larger than c. 10 nm was essentially related to the violent dissolution of Ni; therefore, the intrinsic catalytic activity rapidly decreased during the oxygen reduction process, resulting in severe attenuation of catalyst ORR performance (Figure 1.2).

#### 1.2.2.2 Supported-Enhanced Catalysts

Although carbon support materials are used as commercial catalysts for their excellent performance, carbon corrosion at high electrode potentials can inevitably cause the detachment of Pt NPs from the support, resulting in loss of ORR performance [56–58]. Furthermore, catalytic activity area reduction is due to the migration and aggregation of the supported Pt NPs [59, 60]. Recently, highly graphitized carbon materials such as carbon nanofibers, graphene, and nanotubes attracted the interest of many scientists for these great excellent carbon corrosion resistance [61]. Pt interacts with the rich π site of the graphitized carbon surface, which helps to inhibit the aggregation and oxidation of Pt. Further designing the nanostructures of these highly graphitized carbon materials offers the potential to simultaneously control and improve several properties [62]. Yu Jong-Sung et al. explored methods for supporting high-load Pt NPs and prepared ordered hierarchical nanostructured carbon (OHNC) by reverse replication of silica templates [63]. Compared to carbon black-supported Pt, the catalytic activity of the OHNC-support one was remarkably improved for ORR performance. Keith P. Johnston and coworkers prepared an ordered graphitized mesoporous carbon for ORR with the highly stable Pt supported on it [64]. They found that Pt dissolution, ripening, and coalescence could be mitigated by the electrical contact between the metal and carbon. Ferdi Schüth and

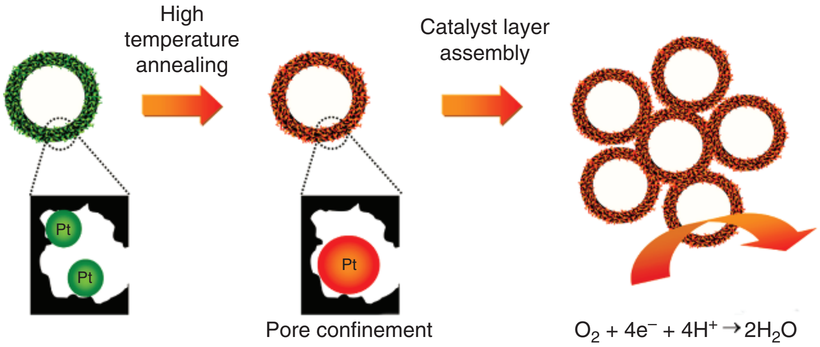

**Figure 1.3** Schematic model of Pt encapsulation by pore confinement. Source: Reproduced with permission of Carolina et al. [65], American Chemical Society.

coworkers developed a form of graphite hollow spheres (HGSs) with mesoporous graphitic carbon [65]. Figure 1.3 shows the principle model of Pt encapsulation prepared by the pore confinement method. Pt NPs with size <2 nm are formed under 30% $H_2$ in Ar at 250 °C. After annealing at a high temperature to 900 °C, Pt NPs grow in the HGS and are limited to about 3–4 nm. HGS with a specific surface area and the precisely controlled pore structure exhibited the long-term stability of the catalyst and maintain high activity.

Although the intrinsic corrosion rates of the above-described nanocarbon materials are reduced several times, they still cannot prevent irreversible carbon oxidation at high potentials. In recent years, several research groups have studied the electrocatalytic systems of Pt NPs supported by non-carbonaceous materials such as tungsten carbide (WC) [66], $WO_x$ [67], $TiO_2$ [68], TiC [69], and ITO [70]. Their results showed that the strong metal-support interaction (SMSI) between supporting materials and Pt NPs could obviously promote the electrocatalytic activities of Pt. It is generally believed that SMSI can greatly affect the activity and durability of by electronic state or Fermi level of Pt NPs to move up and down [71]. For instance, Hwang and coworkers reported a novel functionalized catalytic Pt supported on $Ti_{0.7}Mo_{0.3}O_2$ [71]. The $Ti_{0.7}Mo_{0.3}O_2$ carrier had an electron transfer mechanism from $Ti_{0.7}Mo_{0.3}O_2$ to Pt. Moreover, Pt/$Ti_{0.7}Mo_{0.3}O_2$ possessed much higher stability than Pt/C due to the presence of SMSI between $Ti_{0.7}Mo_{0.3}O_2$ and Pt. Although many non-carbonaceous materials have great promise in the preparation of ORR high-efficiency electrocatalytic systems, some obstacles that inhibit the catalytic performance of oxygen reduction (such as low specific surface area and poor conductivity) still need to be under further investigation. As shown in Figure 1.4b, Wei and coworkers reported that the functionalized $Ti_3AlC_2$ support material (Figure 1.4a) had excellent electrical conductivity comparable to carbon black [72, 73]. Density functional theory (DFT) calculations demonstrated that the changes of electronic structure for Pt NPs in Pt/$Ti_3AlC_2$. The catalytic activity of Pt/e-$Ti_3AlC_2$ (TAC) was not significantly decreased after the durability test by half-wave potential evaluation (Figure 1.4c).

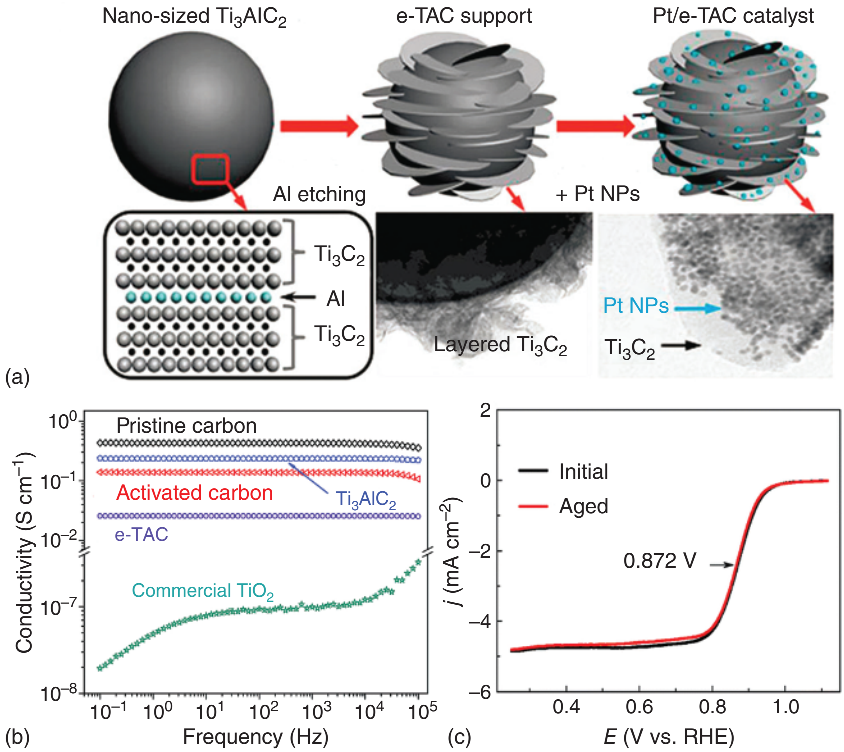

**Figure 1.4** (a) Schematic of Pt/e-TAC catalyst formation. (b) Electrical conductivity of pristine carbon, activated carbon, commercial $TiO_2$, pristine $Ti_3AlC_2$, and e-TAC support. (c) ORR polarization curves for Pt/e-TAC before and after the accelerated durability tests (ADT) cycling (recorded in $O_2$-saturated 0.1 M $HClO_4$ at 1600 rpm and with a scan rate of 10 mV s$^{-1}$). Source: Reproduced with permission of Xie et al. [72], The Royal Society of Chemistry.

**Figure 1.5** (a) Scanning electron microscopic (SEM) and (a-1) high-resolution transmission electron microscopy (HRTEM) images of Fe@N-C-700. (a-2) Discharge-charge polarization curves of rechargeable ZABs with Fe@N-C, Pt/C, and $IrO_2$. (a-3) Cycling performance of rechargeable ZAB with Fe@N-C-700 at 10 mA cm$^{-2}$. Source: Reproduced with permission of Wang et al. [74], Elsevier. (b) Schematic illustration of the preparation process for the Fe-N/C catalyst. (i) An iron ion (ii) btcpb ligand (iii) coordinated Fe-btcpb precursor was formed through a simple solvothermal method (Step I); for clarity, a piece of the 2D network building block is shown in the enlarged view. Then, the Fe-btcpb precursor was pyrolyzed in argon at different temperature for 1 h (Step II), followed by etching in 6 M HCl solution to produce the self-supporting Fe-N/C catalysts (Step III). Galvanostaticdischarge curves of primary ZABs with Fe-N/C-700 and Pt/C as cathode catalysts at current density of (b-1) 5 mA cm$^{-2}$ and (b-2) 20 mA cm$^{-2}$. (b-3) Specific capacities of the ZABs using Fe-N/C-700 and Pt/C as ORR catalysts, which are normalized to the mass of the completely consumed Zn. (b-4) Long-time durability of the primary ZAB using Fe-N/C-700 catalyst at a current density of 5 mA cm$^{-2}$. The battery was recharged by refueling the Zn and the electrolyte for five cycles. Source: Reproduced with permission of Yang et al. [75], WILEY-VCH. (c) Schematic illustration of the synthetic method for Fe, N embedded interconnected MOF-derived porous carbon nanotubes based on tellurium nanotubes as a sacrificial template. (c-1) Porous tellurium nanotubes (Te NT), (c-2) ZIF-8 wired Te NT (Te NT@ZIF-8), (c-3) Fe, N embedded, polydopamine coated Te NT@ZIF-8, and (c-4) Fe, N-embedded, highly graphitic layer coated porous carbon nanotubes after the pyrolysis process at 950 °C for 3 h under argon flow. Source: Reproduced with permission of Ahn et al. [76], WILEY-VCH.

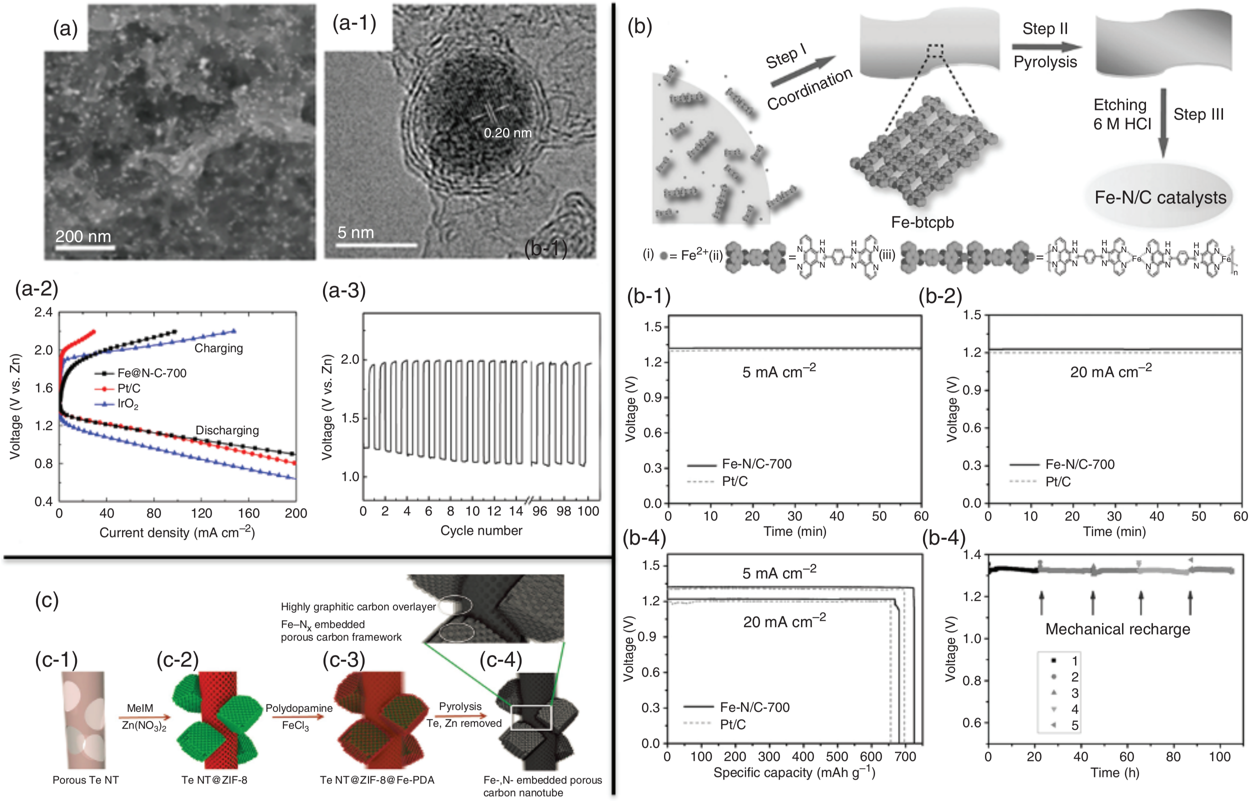
(a)
200 nm
(a-1)
0.20 nm
5 nm
(b-1)
(a-2)
Voltage (V vs. Zn)
Current density (mA cm$^{-2}$)
Charging
Discharging
Fe@N-C-700
Pt/C
IrO$_2$
2.4
2.0
1.6
1.2
0.8
0.4
0
40
80
120
160
200
(a-3)
Voltage (V vs. Zn)
Cycle number
2.0
1.5
1.0
0 2 4 6 8 10 12 14 96 98 100
(b)
Step I
Coordination
Step II
Pyrolysis
Etching
6 M HCl
Step III
Fe-N/C catalysts
Fe-btcpb
(i) ● = Fe$^{2+}$(ii)
(iii)
(b-1)
5 mA cm$^{-2}$
Voltage (V)
Time (min)
Fe-N/C-700
Pt/C
(b-2)
20 mA cm$^{-2}$
Voltage (V)
Time (min)
Fe-N/C-700
Pt/C
(b-4)
5 mA cm$^{-2}$
20 mA cm$^{-2}$
Voltage (V)
Specific capacity (mAh g$^{-1}$)
Fe-N/C-700
Pt/C
(b-4)
Mechanical recharge
Voltage (V)
Time (h)
1
2
3
4
5
(c)
Highly graphitic carbon overlayer
Fe–N$_x$ embedded porous carbon framework
(c-1)
(c-2)
(c-3)
(c-4)
MeIM
Zn(NO$_3$)$_2$
Polydopamine
FeCl$_3$
Pyrolysis
Te, Zn removed
Porous Te NT
Te NT@ZIF-8
Te NT@ZIF-8@Fe-PDA
Fe-,N- embedded porous carbon nanotube

## 1.3 Transition-Metal-Based Materials

### 1.3.1 Metals and Alloys

Although Pt-based nanocatalysts have the best ORR activity, the high cost, and scarcity, Pt hinders their wide practical applications. Therefore, in recent years, high electrocatalytic activity, low cost, and durability of non-noble metal catalysts have been extensively studied. Among them, materials based on Fe, Co, and Ni are the most widely used in ORR catalysts. Xinhe Bao et al. reported a solid-phase precursor's pyrolysis method for the synthesis of Fe NPs encapsulated within N-doped carbon nanoshell with ammonium ferric citrate and dicyandiamide as the precursors (Figure 1.5a, a-1) [74]. In application to ZABs, the Fe@N-C material showed high activity for ORR (Figure 1.5a-2) and excellent durability (Figure 1.5a-3) in the alkaline medium. An-Wu Xu and coworkers developed a pyrolysis strategy of iron coordination complex to prepare a highly active self-supporting Fe-N/C catalyst (Figure 1.5b) [75]. Compared with Pt/C, the Fe-N/C-700 showed the remarkable ORR activity under both alkaline and acidic electrolyte, as well as the excellent ZAB performance when used Fe-N/C-700 as the cathode catalyst (Figure 1.5 (b-1)–(b-4)). Arumugam Manthiram et al. synthesized hierarchically porous 1D carbon nanotube (CNT) with the metal–organic framework (MOF) engaged using porous tellurium nanotubes as a template (Figure 1.5 (c-1)–(c-4)) [76]. Furthermore, the highly effective $FeN_xC$ active sites combined with the hierarchically porous 1D structure were in charge of superior ORR catalytic activity and excellent ZAB discharge performance. Shichun Mu and coworkers prepared Fe, N, and S-codoped carbon nanotubes (Fe/N/S-CNTs) for an efficient ORR catalyst from MOFs treated with hydrazine hydrate and ferrous sulfate [77]. The resulted Fe/N/S-CNT catalyst exhibited a more positive half-wave potential of 0.887 V than that of Pt/C (0.845 V) in the alkaline medium.

Co NPs supported on nanocarbon have also been widely developed as ORR electrocatalysts. Guang Li and coworkers developed a one-pot pyrolysis strategy of the mixture of Co precursor to in situ synthesize Co, N encapsulated carbon nanotubes between the carbon nanosheets (Co-NCNT/Ng) with dicyandiamide and glucose as precursors [78]. The Co-NCNT/Ng with hierarchical porous and high specific surface area exhibited remarkable ORR catalytic activities, including long-term stability, and the high half-wave potential of 0.825 V. When used Co-NCNT/Ng as the air cathode catalyst for ZABs, it exhibited better performance in these respects of long-term stability and power density. Xinhe Bao and coworkers developed a simple strategy to synthesize N-doped carbon nanotube (NCNT) encapsulating Co NPs using dicyandiamide and cobalt-substituted perfluorosulfonic acid/polytetrafluoroethylene copolymer (Co@N-CNT) [79]. In application to ZABs as air cathode catalyst, the Co@N-CNT-8 catalyst exhibited excellent performance and durability due to its great ORR catalytic activity and strong stability in the alkaline medium. Ji-Cai Liang and coworkers demonstrated a simple one-step pyrolysis process to encapsulate Co NPs into N-doped graphene nanoshells [80]. The optimized Co-30@N-G catalyst exhibited an excellent ORR activity comparable

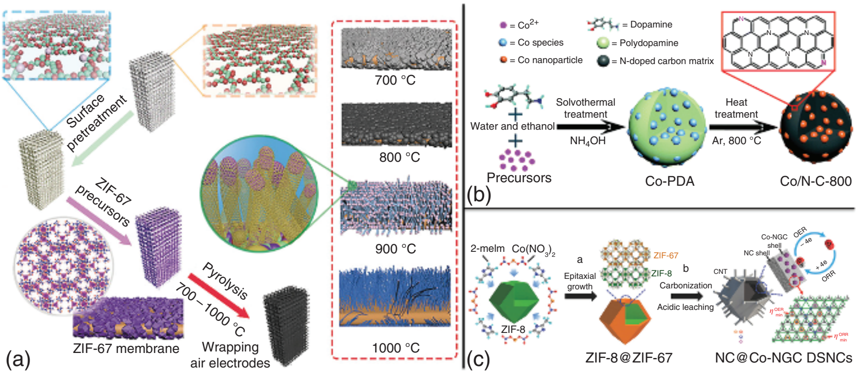

**Figure 1.6** (a) Illustration of the synthesis process for the melamine sponge (MS) zeolite imidazolate framework (ZIF)-T (T=thermal treatment temperature) electrocatalysts. Source: Reproduced with permission of Jia et al. [81], Wiley-VCH. (b) Illustration of the fabrication process for Co/N-C-800. Source: Reproduced with permission of Su et al. [82], The Royal Society of Chemistry. (c) Schematic illustration of the synthesis of NC@Co-NGCDSNCs. Source: Reproduced with permission of Liu et al. [83], © WILEY-VCH.

to Pt/C in an alkaline medium. Moreover, ZAB assembled with Co-30@N-G as the air cathode electrocatalyst showed a high peak power density of 227 mW cm$^{-2}$ with a large current density of 131 mA cm$^{-2}$, as well as a superior specific capacity of 671 mAh $g_{Zn}{}^{-1}$. Degang Fu and coworkers presented a simple pyrolysis strategy of a ZIF-67 thin film on a macroporous polymeric substrate with 3D hierarchical architectures (Figure 1.6a) [81]. They synthesized vertically aligned NCNTs from a surface-mounted MOF as electrocatalysts for ORR and overall water splitting. Zhu Yihua and coworkers reported a hybrid composite material in which Co NPs were encapsulated in N-doped carbon (Co/N-C) [82]. Co/N-C exhibited high catalytic activity for ORR due to the synergistic effect of Co NPs and N-doped carbon in the hybrid material (Figure 1.6b). Jieshan Qiu and coworkers reported a novel process to synthesize double-shelled hybrid nanocages in which N-doped microporous carbon (NC) as inner shells and Co-N-doped graphitic carbon (Co-NGC) as outer shells [83]. When the NC@Co-NGC nanocages were used in ZABs as air electrode catalysts, it exhibited superior electrocatalytic properties to Pt/C with enhanced diffusion kinetics due to its high bifunctional catalytic activity (Figure 1.6c).

Furthermore, transition metal alloys with well-defined electronic structures have also been widely used as high-efficiency electrocatalysts. Tian-Yi Ma and coworkers developed a novel oxygen electrocatalyst in which the bamboo-like N-doped graphitic carbon nanotubes (N-GCNTs) were grown in situ with the bimetal FeCo NPs encapsulated in [84]. In the carbonization process, the metal salts ($Fe(NO_3)_3$ and $Co(NO_3)_2$) were decomposed and turned into alloy nucleus with the temperature reaching 500 °C. Meanwhile, glutamic acid and melamine were pyrolyzed into graphitic carbon and g-$C_3N_4$. With the temperature further increases to 800 °C, the N-GCNTs grew on the graphitic carbon with heteroatom doped under the catalysis of the active metal nucleuses to generate N-GCNT/FeCo. This catalyst demonstrated a high half-wave potential of 0.92 V vs. RHE toward ORR. Furthermore, when the synthesized N-GCNT/FeCo was used as the air electrode in ZABs, it showed superior discharging–charging potential performance, high flexibility, and long lifetime. Francis Verpoort and coworkers synthesized Co-N-CNT catalyst using a facile, low-cost, and scalable approach that pyrolyzing 2D leaf-like ZIF-L [85]. ZABs using the resultant Co-N-CNTs as air electrodes exhibited excellent performance due to their ultrahigh activity for ORR (Figure 1.7a). Wei Xing and coworkers prepared an oxygen catalyst in which the thin graphene nanosheets were coupled with transition metal NPs (TMs@NC$_x$) with a high-loading (~25 wt%) using a unique two-stage encapsulation strategy [86]. The optimal NiFe@NC$_x$ catalyst exhibited high activity with an onset potential of 1.03 V for ORR (Figure 1.7b). John B. Goodenough and coworkers synthesized an oxygen catalyst (NiCo/porous fibrous carbon [PFC] aerogels) in which NiCo NPs immobilized on fibrous carbon aerogel (Figure 1.7c) and showed excellent performance when applied in ZABs [87].

### 1.3.2 Transition Metal Oxides/Sulfides

Transition metal compounds including sulfides, oxides, etc. are considered as alternative non-noble metal catalysts because of their environmental friendliness, low cost, and considerable high activity in alkaline electrolytes. Transition metal oxides are a series of promising non-noble metal catalysts for ORR in alkaline electrolyte. Zhongwei Chen and coworkers synthesized an oxygen catalyst ($MnO_2$-NCNT) derived from NCNTs and manganese dioxide ($MnO_2$) nanotubes for ORR [88]. When the $MnO_2$-NCNT composite having excellent ORR activities in the alkaline medium was used as an air cathode of a ZAB, it exhibited excellent discharge performance as well as strong stability. Rongfang Wang and workers embedded MnO NPs in nitrogen-doped mesoporous carbon (MnO/NC) as catalysts for the ORR and ZABs [89]. NaCl used as template has significant effect on mesoporous carbon material. The assembled ZAB exhibited an open-circuit voltage of 1.49 V, and a peak power density of 168 mW cm$^{-2}$ at a current density of about 200 mA cm$^{-2}$.

In terms of cobalt-based oxides, Dai and coworkers found that covalent hybridization of cobalt oxide (e.g. CoO, $Co_3O_4$) with CNT or graphene oxide could significantly increase ORR activity [90, 91]. The strong coupling between the highly graphitized carbon support and the oxidized NPs promoted the high catalytic activity of such composite materials. Jun Lu and coworkers fabricated an oxygen catalyst consisting of a layer of atomic thin mesoporous $Co_3O_4$/N-doped reduced graphene oxide (rGO) (N-rGO) nanosheets [92]. The oxygen catalyst had mesoporous structure, high specific surface area, strong synergistic effects between $Co_3O_4$ and N-rGO nanosheets, and high activity and strong durability for ORR. Moreover, the assembled knittable fiber-shaped ZAB exhibited enhanced and stable electrochemical performance (Figure 1.8). Metal oxide nanoarrays are considered to be alternative options for the affordable, efficient electrocatalysts of PEMFCs and ZABs. As shown in Figure 1.9a an alternative strategy for preparing ORR catalysts by coating three-dimensional CoO$_x$ nanoarrays with porous N-doped carbon layer (CoO$_x$@NC nanoarray) was proposed by Xiaoming Sun and coworkers [93]. Porous NC not only provided a conductive coating that facilitated charge

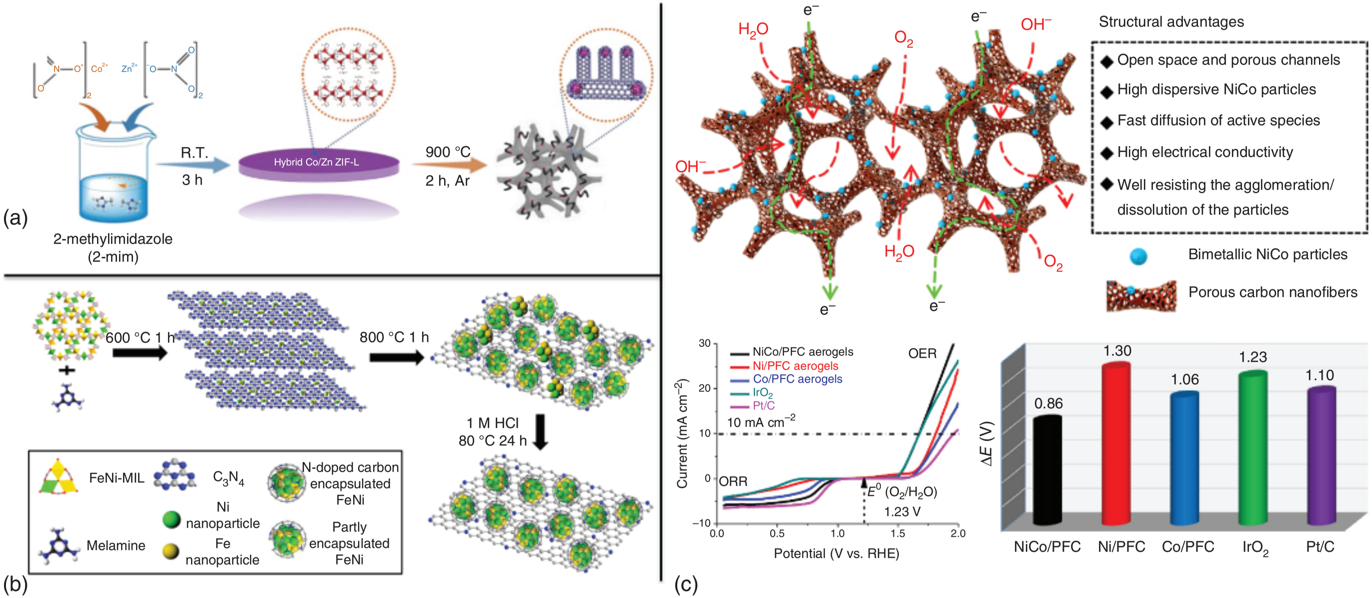

**Figure 1.7** (a) Schematic illustration toward the synthetic process of Co-N-CNTs. Source: Reproduced with permission of Wang et al. [85], WILEY-VCH. (b) Schematic illustration of the synthetic strategy of the TMs@NC$_x$ composite. Source: Reproduced with permission of Zhu et al. [86], American Chemical Society. (c) Schematic illustration of the advantages of the NiCo/PFC aerogels as electrocatalysts. Source: Reproduced with permission of Fu et al. [87], American Chemical Society.

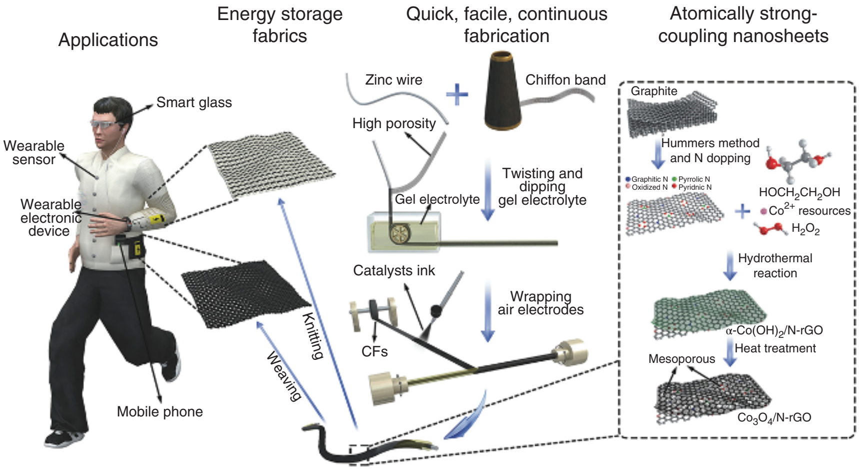

**Figure 1.8** Schematic illustration to the fabrication process of a flexible fiber-shaped ZAB as well as atomically thin mesoporous $Co_3O_4$/N-rGO hybrid nanosheets with 2D layer-by-layer structure. Source: Reproduced with permission of [92], WILEY-VCH.

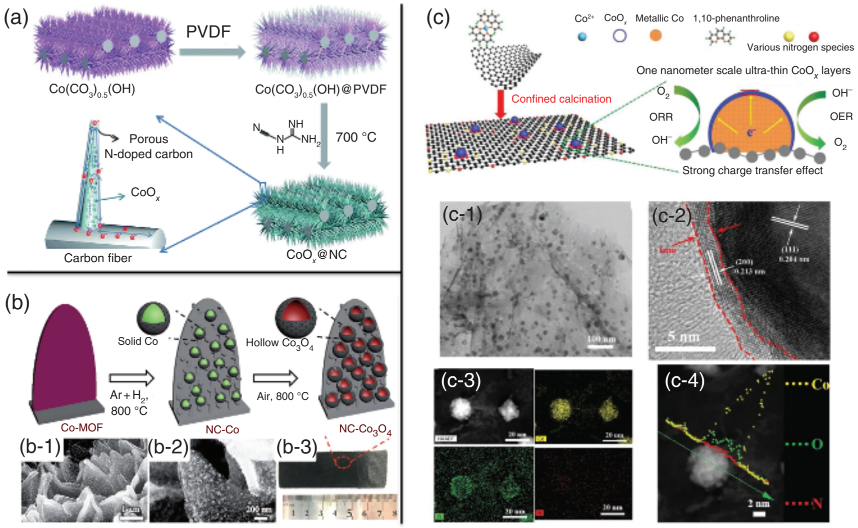

**Figure 1.9** (a) The schematic diagram of the preparation of the $CoO_x$@NC nanoarray. Source: Reproduced with permission of Hao et al. [93], Royal Society of Chemistry. (b) Schematic illustration of the fabrication process for hierarchical NC-$Co_3O_4$ arrays on flexible carbon cloth. (b-1, b-2) SEM and (b-3) digital images of NC-$Co_3O_4$ nanoarrays on carbon cloth. Source: Reproduced with permission of Guan et al. [94], WILEY-VCH. (c) Schematic illustration of 1 nm-$CoO_x$ layer on the metallic substrate of Co/N-rGO. (c-1) TEM image. (c-2) HRTEM image. (c-3) high-angle annular dark field scanning transmission electron microscopy (HAADF-STEM) image and corresponding elemental images. (c-4) Line-scan energy-dispersive spectroscopy (EDS) elemental distribution curves of Co, O, and N in the 1 nm-$CoO_x$ layer on the Co/N-rGO catalyst. Source: Reproduced with permission of Zhou et al. [95], WILEY-VCH.

transfer and retention of electrolyte diffusion channels but also greatly increased the electrochemical surface area. In application to rechargeable ZABs as an air cathode, the electrode exhibited better durability than Pt/C. John Wang and coworkers embedded hollow $Co_3O_4$ nanosphere into nitrogen-doped carbon nanowire arrays on flexible carbon cloth to prepare a highly efficient oxygen catalyst (NC-$Co_3O_4$/CC) derived from a Co-based MOF precursor (Figure 1.9b) [94]. The irregular hollow $Co_3O_4$ nanospheres having a fine scale NP structure (Figure 1.9b-1, b-2) were formed by the Kirkendall effect. When NC-$Co_3O_4$/CC was used as a self-supporting air cathode catalyst (Figure 1.9b-3) for a flexible ZAB, it exhibited high capacity (387.2 $mAh\,g^{-1}$), outstanding stability, and remarkable flexibility. As shown in Figure 1.9c, Changzheng Wu and coworkers synthesized a 1 nm-scale $CoO_x$ layer on a metallic Co/N-doped graphene (Figure 1.9(c-1)-(c-4)) [95]. The results showed that the ultrathin $CoO_x$ layer enabled accelerated electron conduction and provided abundant active sites. Besides, the N-doped graphene substrate and metallic Co core also promoted electron transfer, resulting in remarkable electrocatalytic activity for ORR in alkaline medium.

Mixed valence oxides of transition metals with a spinel structure are considered to be a vital class of metal oxides. In particular, substituted $Co_3O_4$ with Mn, Ni, and Cu has shown excellent activity and strong stability toward ORR [96]. Yucheng Lei and coworkers developed $NiCo_2O_4$ nanosheet with spinel structure and oxygen defects [97]. This catalyst with the oxygen vacancies and numerous active sites exhibited remarkable ORR performance with an onset potential of 0.85 V vs. RHE. When used in ZABs, it exhibited the high power density of 102.08 $mW\,cm^{-2}$ comparable to Pt/C. Yuan Chen and coworkers synthesized a series of hybrid materials composed of amorphous bimetallic oxide NPs immobilized on the surface of N-rGO [98]. With the aid of N-containing polyethyleneimine (PEI) polymer binder, Prussian blue or FeCo Prussian blue analog nanocrystals having a size of about 5 nm were first grown on the surface of graphene oxide (GO). At the optimized oxidative decomposition temperature, the Prussian blue (PB)/Prussian blue analogue (PBA) nanocrystals were converted into amorphous $Fe_aCo_{1-a}O_x$ nanocrystals ($0 \leq a \leq 1$) and the polymer/graphene oxide was simultaneously converted into N-rGO. $Fe_{0.5}Co_{0.5}O_x$ exhibited excellent oxygen catalytic activity with a large limiting current density for ORR. The assembled ZAB had a specific capacity of 756 $mAh\,{g_{Zn}}^{-1}$ and a peak power density of 86 $mW\,cm^{-2}$. Haipeng Yang and coworkers prepared a $NiCoO_2$/graphene complex having a highly ordered 3D porous cellular network as ORR/oxygen evolution reaction (OER) electrocatalysts with the presence of the sodium dodecyl sulfate (SDS) anion surfactant [99]. The as-prepared catalyst demonstrated durable catalytic activities with a high half-wave potential for ORR. The experimental results exhibited that the catalyst had a high specific surface area due to its highly ordered three-dimensional structure and there was a strong bridging bond between $NiCoO_2$ nanosheets and flake graphene, which resulted in the good electrocatalytic activity.

Transition metal sulfides, various combinations of transition metal sulfides, and transition metals (Fe, Co, etc.) have been confirmed to have high activity for ORR. Furthermore, the surface electronic structure configuration can be optimized by doping the heteroatoms (such as S, N, P) into the carbon framework to promote the adsorption/desorption behavior of the oxygen intermediate, thereby promoting the electrocatalytic kinetic processes [100]. Among them, cobalt sulfides have drawn more attention in ORR [101–103]. Yang Yang and coworkers prepared $TiO_2$ nanoporous film material embedded in N, P codoped $CoS_2$ nanoclusters (N, $P/CoS_2@TiO_2$) (Figure 1.10a-(a-3)) to enhance electrochemical activities for ORR [104]. They found that both N and P doping can improve the properties of the material, wherein the conductivity and electrochemical activity of the nanoporous film can be effectively improved by N-doping, while P-doping can passivate the surface of the electrode and improve stability. In application to two tandem ZABs, the N, $P/CoS_2@TiO_2$ nanoporous films (NPFs) exhibited the excellent discharge potential (2.19 V), open-circuit voltage (2.37 V), and a strong stability for discharge over 130 hours (Figure 1.10a-4). The combination of carbonaceous nanomaterials and active species has been proven to improve the electrical conductivity by improving overall conductivity and coupling synergies. Jian Zhang and coworkers synthesized $Co_9S_8$ NPs loaded onto a N, S co-implanted 3D carbon matrix ($Co_9S_8@NSCM$) as a highly active electrocatalyst for ORR in alkaline solution [107]. The bimetallic zeolite imidazolate framework (ZIF) constructed by reacting Co(II) and Zn(II) ions with 2-methyl-imidazolate (MeIm) in methanolic solution was converted to a uniform heteroatom doped orderly carbon matrix under high temperature calcination.

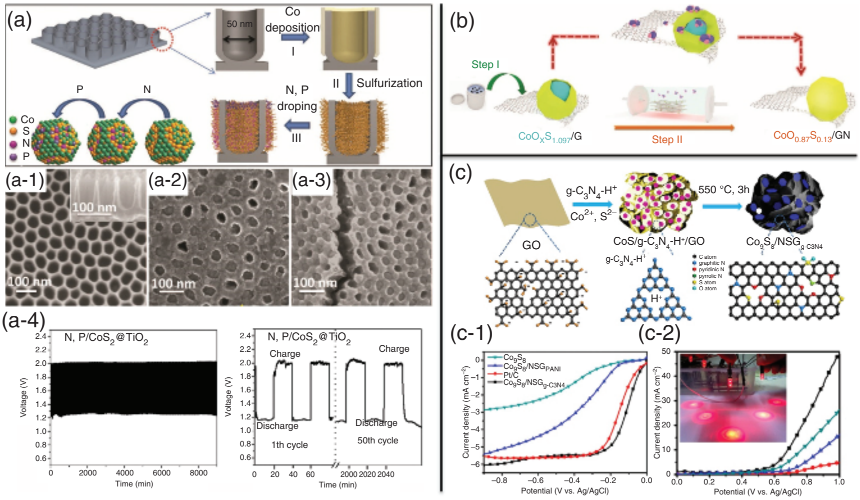

**Figure 1.10** (a) Fabrication process of the $N,P/CoS_2@TiO_2$ NPFs. SEM images of pristine (a-1) $TiO_2$ NPFs, (a-2) $CoS_2@TiO_2$, and (a-3) N, $P/CoS_2@TiO_2$, respectively. (a-4) Discharge–charge profiles of ZABs composed with N, $P/CoS_2@TiO_2$ catalysts at a current density of 10 mA $cm^{-2}$ at room temperature. Source: Reproduced with permission of Guo et al. [104], WILEY-VCH. (b) Schematic illustration of the synthesis of $CoO_{0.87}S_{0.13}/GN$. Source: Reproduced with permission of Fu et al. [105], John Wiley and Sons. (c) Schematic demonstration of the preparation process for $Co_9S_8/NSG_{g\text{-}C_3N_4}$. linear sweep voltammograms (LSV) polarization curves for (c-1) ORR and (c-2) OER of $Co_9S_8/NSG_{g\text{-}C_3N_4}$, $Co_9S_8/NSG_{PANI}$, $Co_9S_8$, and commercial Pt/C catalysts in $O_2$-saturated 0.1 M KOH in the range of 0.0 - 1.0 V vs. Ag/AgCl (inset shows the digital image of the LEDs lighted by the ZAB). Source: Reproduced with permission of Tang et al. [106], American Chemical Society.

Meanwhile, $Co_9S_8$ NPs can be grown in situ on the carbon substrate under a sulfur vapor atmosphere. Owing to the optimized synergistic effect between the $Co_9S_8$ and N, S co-implanted 3D carbon matrix (NSCM) interface, the $Co_9S_8$@NSCM exhibited remarkable stability and discharge performance in ZABs. Zhongwei Chen and coworkers synthesized S-deficient cobalt oxysulfide single crystals immobilized on N-doped graphene nanomeshes ($CoO_{0.87}S_{0.13}$/graphene nanomeshes [GN]), which can be directly used in PEMFCs and ZABs as a freestanding catalyst film [105]. They found that the edge-nitrogen-rich GN produced by ammonolysis not only provided intimate electronic contact with $CoO_{0.87}S_{0.13}$ NPs but also provided short diffusion channels and adequate open space for intermediates and reactants in the electrocatalysis process (Figure 1.10b). When compared to Pt/C, $CoO_{0.87}S_{0.13}$/GN has performed better performance regarding onset potential ($E_{\text{onset}} = 0.94\,\text{V}$ vs. RHE), half-wave potential ($E_{1/2} = 0.83\,\text{V}$ vs. RHE), and the diffusion-limiting current ($4.12\,\text{mA cm}^{-2}$@0.7 V). More significantly, $CoO_{0.87}S_{0.13}$/GN shows better ORR stability than the Pt/C catalyst without significant losses in activity after 3000 cycles of cyclic voltammetry between 0.6 and 1.7 V in $O_2$-saturated 0.1 M KOH solution at $50\,\text{mV s}^{-1}$. Dongqing Wu et al. reported a facile ionic assembly strategy to synthesize a hybrid of quasi-hexagonal $Co_9S_8$ nanoplates and S and N dual-doped graphene ($Co_9S_8/NSG_{g\text{-}C_3N_4}$) (Figure 1.10c) [106]. $Co_9S_8/NSG_{g\text{-}C_3N_4}$ demonstrated excellent ORR activity performance with the large limited current density of $6.05\,\text{mA cm}^{-2}$ at −0.9 V vs. Ag/AgCl and the onset potential of −0.02 V vs. Ag/AgCl (Figure 1.10c-1). As shown in Figure 1.10c-2, $Co_9S_8/NSG_{g\text{-}C_3N_4}$ also had significant catalytic activity for OER.

Substituting other dopants for transition metals has proven to be an effective way to enhance the catalytic activity for ORR [108]. John Wang and coworkers synthesized a single-phase bimetallic (Ni, Co)$S_2$ as a highly efficient catalyst for ORR [109]. In application to ZABs, a high peak power density of $153.5\,\text{mW cm}^{-2}$, a high open cell voltage of 1.48 V, and strong discharge stability were obtained (the discharge voltage remained at 1.47 V over 20 hours). Han et al. prepared an efficient oxygen electrocatalyst ($NiCo_2S_4$/N-CNT) in which the homogeneous $NiCo_2S_4$ nanocrystals were supported on NCNTs (Figure 1.11a) [110]. When used as cathodes in rechargeable ZABs, it exhibited enlarged energy efficiency (≈67.2%) (Figure 1.11a-1), high peak power density ($147\,\text{mW cm}^{-2}$ at 0.77 V) (Figure 1.11a-2), and strong stability (Figure 1.11a-3). Aiping Yu and coworkers synthesized urchin-like $NiCo_2S_4$ microsphere synergized with S-doped graphene nanosheets (sulfur-doped graphene nanosheets [S-GNS]/$NiCo_2S_4$) (Figure 1.11b-(b-2)) [111]. The resulted S-GNS/$NiCo_2S_4$ exhibited excellent electrocatalytic activities for ORR in the alkaline medium. Furthermore, in application to ZABs, it demonstrated a maximum power density of $216.3\,\text{mW cm}^{-2}$ and strong stability for 100 hours (Figure 1.11b-3). Its unique structure and morphology, as well as S-GNS and the synergistic effect of $NiCo_2S_4$, led to the remarkable electrocatalytic activity of S-GNS/$NiCo_2S_4$ catalysts. First, nano-needle with microspherical structure well-assembled urchin-like $NiCo_2S_4$, which greatly increased the surface exposure of the active site, giving this morphology an effective mass and charge transport pathway. S-GNS can not only increase the electrical conductivity but also improve

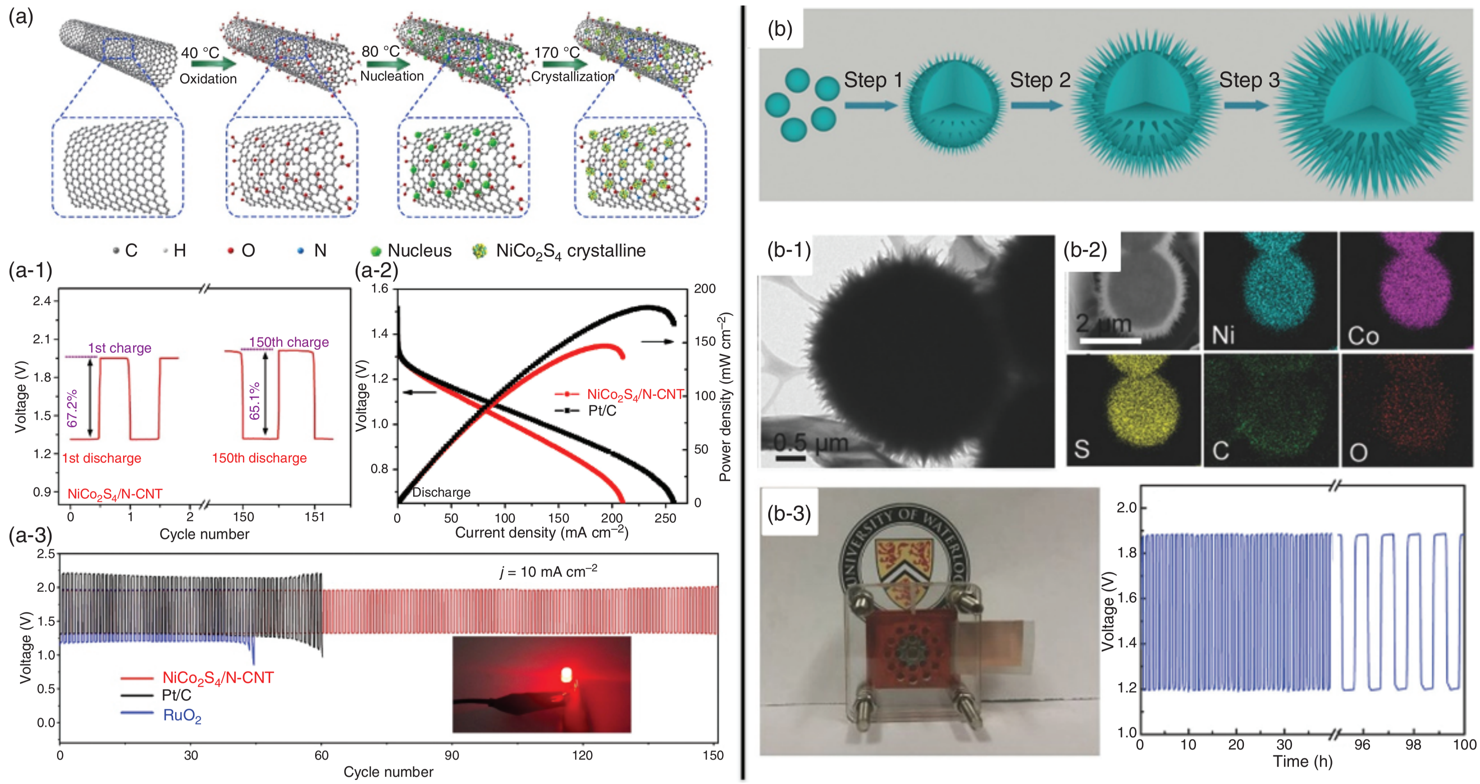

**Figure 1.11** (a) Schematic illustration of the preparation of $NiCo_2S_4$/N-CNT nanocomposite. (a-1) 1st and 150th discharge/charge curves of $NiCo_2S_4$/N-CNT electrode. (a-2) Polarization curves and corresponding power densities of $NiCo_2S_4$/N-CNT and Pt/C-based cathodes. (a-3) Discharge/recharge profiles of rechargeable ZABs based on $NiCo_2S_4$/N-CNT, Pt/C and $RuO_2$ cathode with duration of 400 seconds per cycle at 10 mA $cm^{-2}$. Inset shows a LED light lit by an assembled ZAB. Source: Reproduced with permission of Han et al. [110], Elsevier. (b) Schematic diagram for the evaluation and formation process of urchin-like NiCo-based carbonate hydroxide microsphere. (b-1) Low-magnification TEM images and (b-2) element mappings of nickel, cobalt, sulfur, carbon, and oxygen in the as-obtained S-GNS/$NiCo_2S_4$ nanocomposite. (b-3) Photography of a home-made rechargeable ZABs and galvanostatic charge/discharge test of the home-made ZABs built with S-GNS/$NiCo_2S_4$ catalyst at 10 mA $cm^{-2}$. Source: Reproduced with permission of Liu et al. [111], WILEY-VCH.

the contact between electrolyte and catalyst, and maintain the catalyst integrity during discharge process because of the robustness of graphene nanosheets (GNS), thereby resulting in enhanced the cycle stability. In addition, S-GNS also enhanced the electrocatalytic activity due to the spin density of carbon atoms in the vicinity of heteroatoms caused by sulfur doping (Figure 1.11b).

## 1.4 Atomically Dispersed Metal in Carbon Materials

Since the ORR only occurs on the surface of the NP catalyst, moreover, the key steps in determining the catalytic efficiency are the adsorption of the reactants and the desorption of the product at the active site. Reaction kinetics have been confirmed to be easy to tune by the shape and size of NPs, and the catalytic activity is mainly contributed by surface atoms while the role of the core is minimal. The atomic dispersion of active sites can enhance the chemical interaction with the support and increase utilization efficiency. Recent researchers have proved that the content of the uncoordinated metal atoms being used as catalytic activity sites is increased by the reduction of the size of NPs to the sub-nanometer range [112]. In recent years, the application of single atomic catalysts in energy conversion and storage has attracted widespread attention. The results showed that support matrices not only provide anchor sites for single metal atoms, provide excellent conductivity, but also manipulate metal atoms, electronic structure, and charge density of adjacent carbon atoms [113–115].

The high cost or large consumption of conventional Pt NP-based catalysts is mainly because of the slow ORR dynamics and low Pt utilization efficiency on per Pt atom. Reducing Pt NP to a single atom is one of the most effective approaches to reduce the high consumption of Pt by increasing the efficiency of Pt utilization. Jing Liu et al. developed a Pt single-atom electrocatalyst supported on carbon black (Figure 1.12a) with efficient activity and durable for ORR via a simple optimization procedure with chloroplatinic acid as Pt precursor and urea as N precursor, respectively [116]. The obtained carbon-supported doped-N triggered Pt single-atom catalyst (SAC) with a Pt content of 0.4 wt% has high oxygen reduction activity (Figure 1.12 (a-1)–(a-3)), stability, and tolerance to poisoning in both acid solution and alkaline solution (Figure 1.12a). Ronghai Yu and coworkers reported a new active moiety of $Pt_1$-$O_2$-$Fe_1$-$N_4$ via a precise anchoring a Pt atom to the iron center by bonding with an oxygen molecule (Figure 1.12b) [117]. The results showed that the atomically Pt and Fe-$N_4$ moieties were uniformly dispersed on the carbon support (Figure 1.12b-1), then the reduced oxidation state of Fe coupled with the Fe—O bond in $Pt_1$@Fe-N-C supported the hypothesis of new $Pt_1$-$O_2$-$Fe_1$-$N_4$ (Figure 1.12b-2, b-3). The oxygen reduction catalytic activities of $Pt_1$@Fe-N-C showed a half-wave potential (0.80 V), an onset potential (0.93 V) in $O_2$-saturated $H_2SO_4$ (Figure 1.12b-4), and a peak power density of 0.86 W cm$^{-2}$ at 0.49 V in a real acidic PEMFC (Figure 1.12b-5).

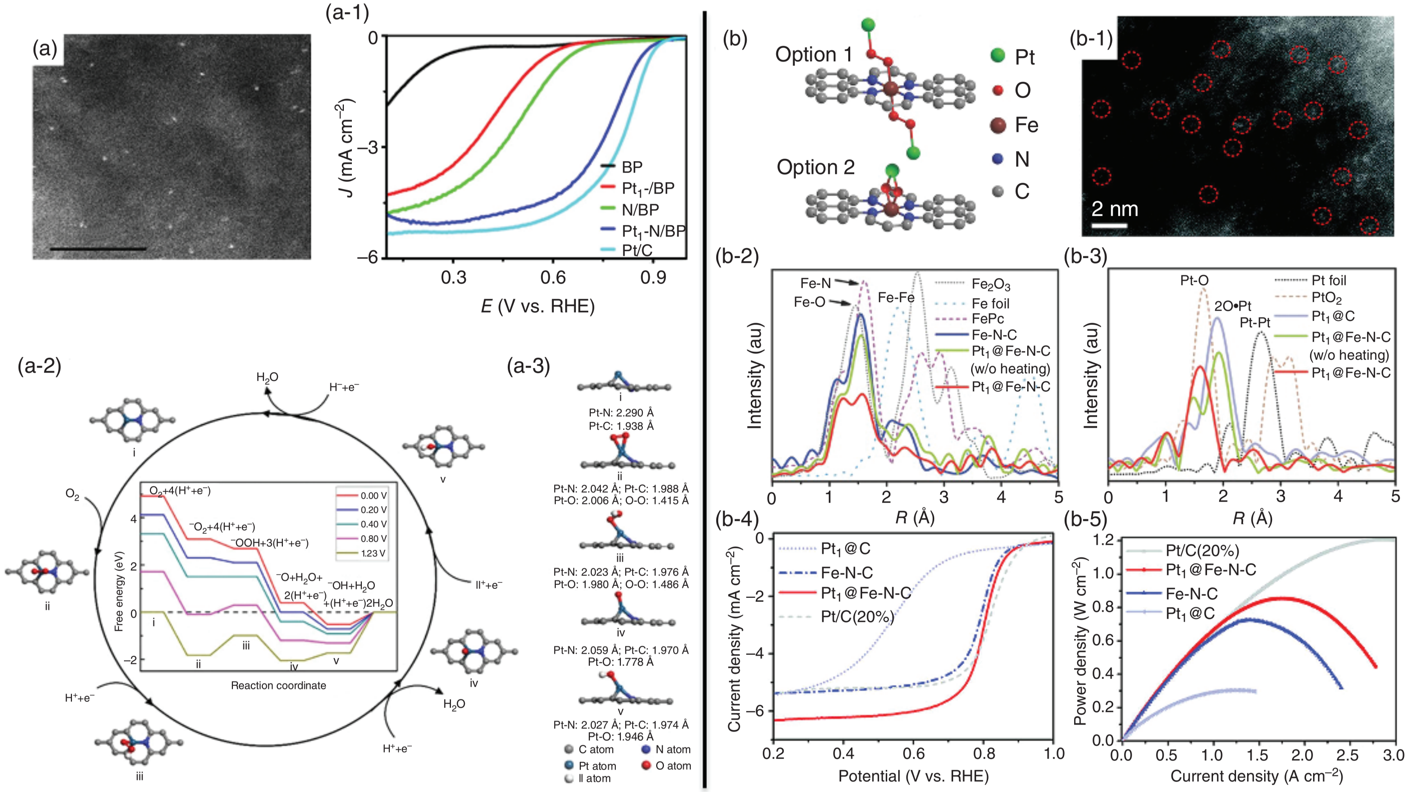

**Figure 1.12** (a) HAADF-STEM images of Pt$_1$-N/black pearls (BP) (carbonblack BP2000), (a-1) rotating ring-disk electrode (RRDE) polarization curves of BP, N/BP, Pt$_1$/BP, Pt$_1$-N/BP, and commercial Pt/C in $O_2$-saturated 0.1 M $HClO_4$ with a scan rate of 5 mV s$^{-1}$ and rotation speed of 1600 rpm, (a-2, a-3) the proposed reaction pathways for complete oxygen reduction reaction on the g-P-N$_1$-Pt$_1$ catalyst. Source: Liu et al. [116], Springer Nature. Licensed under CC BY 4.0. (b) Proposed schematic diagram of Pt$_1$-O$_2$-Fe$_1$-N$_4$-C$_{12}$ as the active moiety of Pt$_1$@Fe-N-C. (b-1) HAADF-STEM image of Pt$_1$@Fe-N-C catalyst. (b-2) Magnitudes of $k_3$-weighted Fourier-transformed extended X-ray absorption of fine structure XAFS (EXAFS) data of Fe in Fe-N-C, Pt$_1$@Fe-N-C (w/o heating), and Pt$_1$@Fe-N-C with references of FePc, $Fe_2O_3$, and Fe foil. (b-3) Fourier-transformed EXAFS data of Pt in the catalysts with references of $PtO_2$ and Pt foil, (b-4) LSV curves of the indicated catalysts measured by RRDE technique in $O_2$-saturated 0.5 M $H_2SO_4$, (b-5) power density curves of membrane electrode assemblies (MEAs) with Fe-N-C, Pt$_1$@Fe-N-C, Pt$_1$@C, and Pt/C (20%) as the cathode catalyst, respectively. Source: Reproduced with permission of Zeng et al. Zeng et al. [117], WILEY-VCH.

The metal–$N_x$ configuration is generally considered to be the active site in metal-doped carbon. Transition-metal-based materials have a wide range of applications in ORR electrocatalysis [118, 119]. Yadong Li and coworkers synthesized isolated single atomic sites anchored on hollow N-doped carbon spheres (ISAS-Co/HNCS) with uniformly dispersed single Co atomic sites by a template-assisted pyrolysis method (Figure 1.13a) [120]. Transmission electron microscopy (TEM) proved ISAS-Co/HNCS retained spherical shape (Figure 1.13a-1) with the wall thickness of roughly 5 nm (Figure 1.13a-2) and the existing form of cobalt single atoms (Figure 1.13a-3, a-4). It possessed excellent oxygen reduction catalytic activity in $H_2SO_4$ solution ($E_{1/2} = 0.773\,\text{V}$) due to its uniformly dispersed single atom cobalt sites, increasing exposure to active sites and hollow substrate resulting in accelerating the mass transfer of related species. Furthermore, a series of ISAS-M/HNCS (M = Fe, Cu, etc.) can be synthesized. Yadong Li and coworkers also synthesized atomic-dispersed Fe anchored on sulfur and nitrogen-codoped carbon (Fe-ISA/SNC) (Figure 1.13b) [121]. The contents of S, N can be broadly adjusted by the initial ratio of polymeric monomers. The oxygen reduction reactivity of Fe-ISA/SNC exhibited a trend of increasing first and then decreasing with the increase of S doping. The optimal Fe-ISA/SNC showed excellent ORR performance that half-wave and onset potentials were more positive than Pt/C (Figure 1.13b). Yadong Li and coworkers also developed a simple pyrolysis process of predesigned bimetallic Zn/Co MOFs to synthesize atomic-dispersed Co on N-doped porous carbon [122]. In this process, the carbonization of the organic linking agent can reduce Co and selectively evaporate Zn. The results of the structural analysis indicated the Co single atoms stabilized by as-resulted N-doped porous carbon (Figure 1.13c).

Jin-Song Hu and coworkers used a cascade anchoring strategy to manufacture M-NC SACs in which M included Co, Mn, Mo, Fe, Cu, Ni, Pt, etc. and metal loadings up to 12.1% [123]. Figure 1.14a shows the preparation procedure of the M-NC SAC electrocatalyst, metal ions were first sequestered by a chelating agent, then anchored onto high surface area porous carbon which had the rich oxygen-containing functional group. Metal ions can be effectively isolated by chelating agents, and chelating agents can also bind to carbon support by the interaction with hydrogen bonding. Excessive chelating agents attached to the surface of support physically separate the metal complex. Then, melamine as a nitrogen source was mixed with the complex bond carbon for subsequent pyrolysis to achieve M-NC SACs. During the pyrolysis process at high temperature (>~600 °C), the carbon-nitrogen species ($CN_x$) (such as $C_3N_4$, etc.) decomposition from melamine can then be combined with metal atoms to form M–$N_x$ to the prevention of metal atom polymerization (Figure 1.14a-1, a-2). The atomically dispersed Fe-NC SAC showed ultrahigh ORR catalytic activity with a kinetic mass current of $100.7\,\text{A g}^{-1}$ at 0.9 V and a half-wave potential of 0.90 V (vs. RHE) in 0.1 M KOH. As shown in Figure 1.14b, Yadong Li and coworkers used an encapsulated-precursor pyrolysis approach to prepare an isolated single-atom Fe-N-C catalyst (Figure 1.14 (b-1)–(b-4)) with excellent ORR reactivity [124]. The half-wave potential of Pt/C appeared at 0.842 V, while the half-wave potential of as-obtained catalyst reached 0.90 V, which manifested that the single-atom Fe-N-C catalyst showed high ORR catalytic activity.

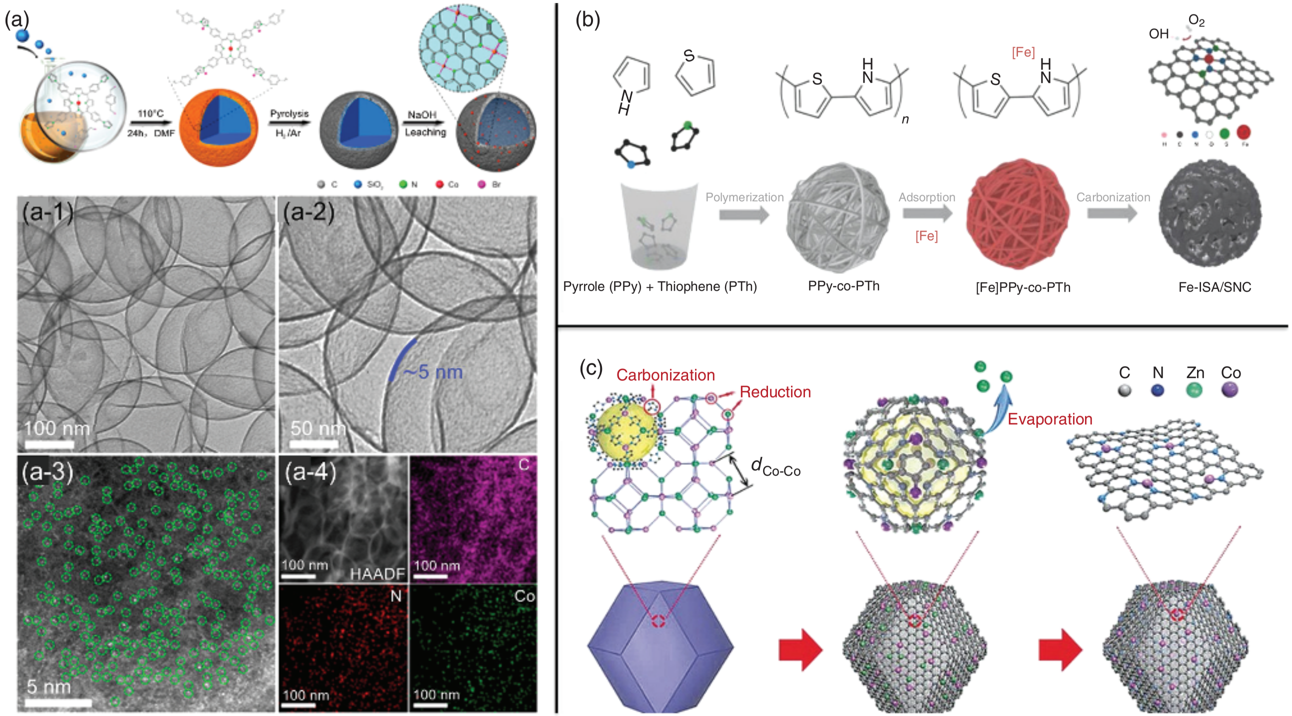

**Figure 1.13** (a) Schematic illustration of the synthesis of ISAS-Co/HNCS. (a-1, a-2) TEM images of ISAS-Co/HNCS. (a-3) AC HAADF-STEM image of ISAS-Co/HNCS; isolated bright dots marked with light-green circles are cobalt atoms. (a-4) HAADF-STEM image and corresponding EDX element mapping of ISAS-Co/HNCS: C (violet), N (red), and Co(green). Source: Reproduced with permission of Han et al. [120], American Chemical Society. (b) Illustration of the synthetic process of Fe-ISA/SNC. Source: Reproduced with permission of Li et al. [121], WILEY-VCH. (c) Scheme of the proposed formation mechanisms for Co SAs/N-C [122]. Source: Reproduced with permission of Yin et al. [122], WILEY-VCH.

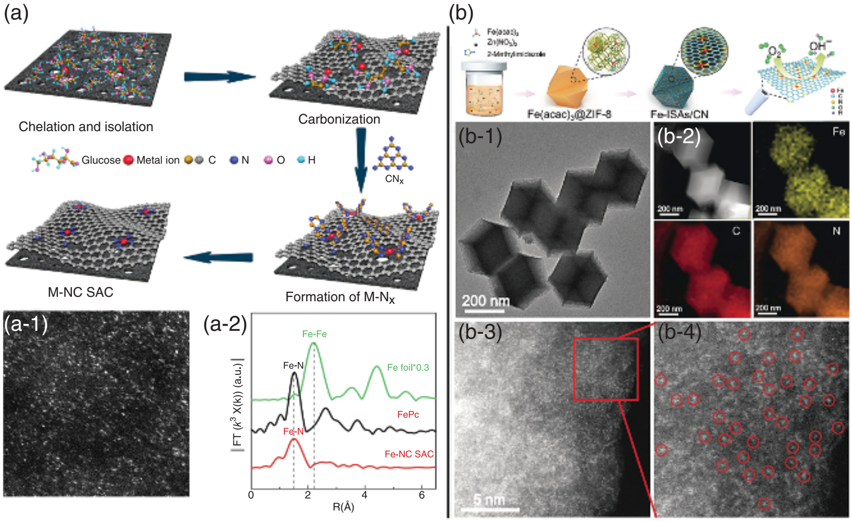

**Figure 1.14** (a) The cascade anchoring strategy for the synthesis of M-NC SACs. (a-1) HAADF-STEM image of Fe-NC SAC. (a-2) Fourier transform of Fe K-edge EXAFS spectra of Fe-NC SAC and reference samples (FePc and Fe foil). Source: Zhao et al. [123], Springer Nature. Licensed under CC BY 4.0. (b) Schematic illustration of the formation of Fe-ISAs/CN, (b-1) TEM, (b-2) HAADF-STEM images, corresponding element maps showing the distribution of Fe (yellow), C (red), and N (orange), (b-3) HAADF-STEM image, and (b-4) enlarged image of the Fe-ISAs/CN. Single Fe atoms are highlighted by red circles [124]. Source: Reproduced with permission of Chen et al. [124], Wiley-VCH.

## 1.5 Metal-Free ORR Electrocatalysts

Graphene, carbon nanotubes, and nanocarbon are by far the most available heteroatom-doped carbon for metal-free ORR electrocatalysts [125]. For instance, since the vertically aligned N-doped carbon nanotubes (VA-NCNTs) for metal-free ORR catalysts were first reported by Dai and coworkers, a large number of other carbon materials related to heteroatom-doped were extensively reported [126–128]. For example, Zhang and coworkers developed an approach for synthesizing two-dimensional N and S double-doped porous carbon nanosheets (N/S-2DPCs) [129]. The N/S concentration determined the ORR catalytic performance of 2DPCs and exhibited the optimal ORR performance when the S/N ratio was 0.05 (N/S-2DPC-60). In addition, they assembled ZABs using N/S-2DPC-60 as an air cathode catalysts. Notably, the results showed that it had remarkable cycling stability for 12 hours at 20 mA cm$^{-2}$. Furthermore, in acidic solution, these nitrogen-sulfur double-doped carbon nanomaterials also had excellent ORR activity [130]. Mullen and coworkers exploited a series of N-doped carbon nanosheets with a pore size of ≈22 nm [131]. This carbon nanosheets displayed significant ORR activities in an acidic solution with an onset potential of 0.72 V vs. RHE and a 4e pathway.

Recently, carbon nanomaterials derived from biomass applying in ORR catalysts have also attracted great attention [132]. For instance, the banana peel was used

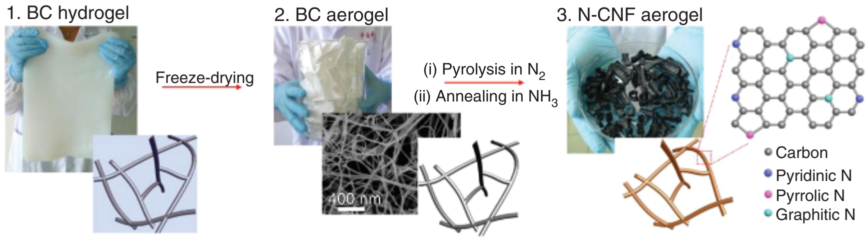

**Figure 1.15** Synthesis and morphologies of N-CNF aerogels. Source: Reproduced with permission of Liang et al. [134], Elsevier.

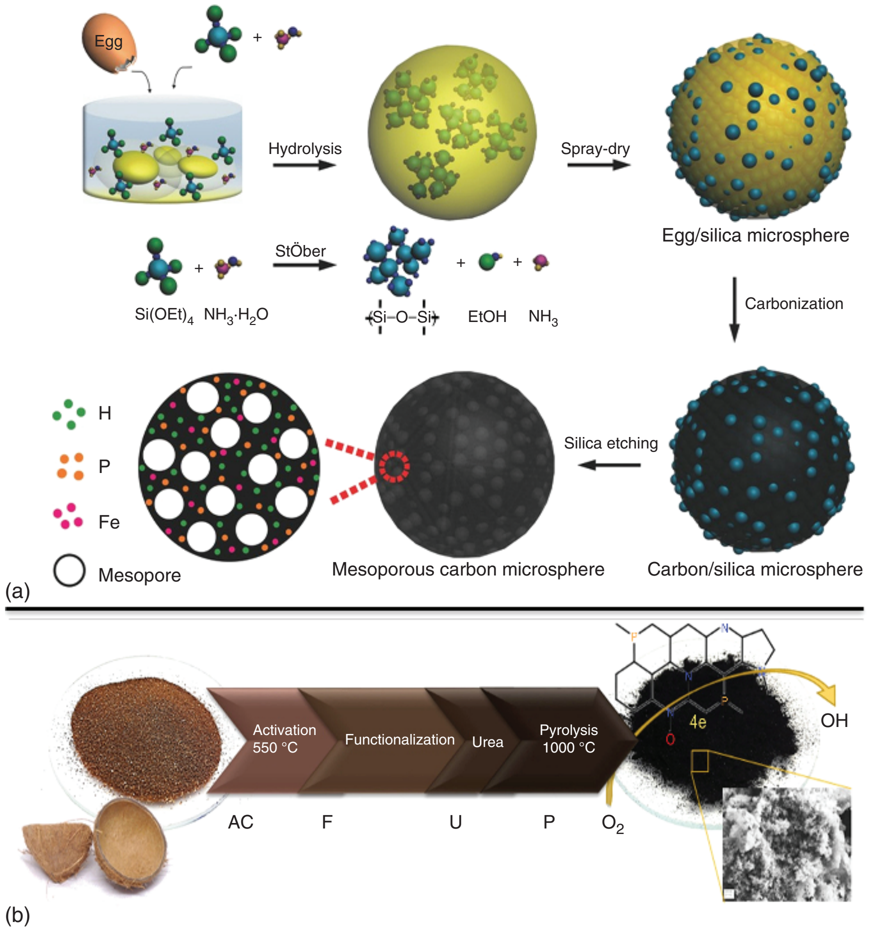

**Figure 1.16** (a) Schematic illustration of the fabrication of egg-CMS. Source: Reproduced with permission of Wu et al. [135], WILEY-VCH. (b) Schematic of the synthesis of N, P-doped porous carbon from coconut shells. Source: Reproduced with permission of Borghei et al. [136], Elsevier.

to prepare 3D porous carbon nanosheets through calcination and KOH activation [133]. In application to a ZAB, the resulting carbon nanosheets had excellent ORR performance and high power density (208 mW cm$^{-2}$). Bacterial cellulose (BC) was also applied to prepare the N-doped carbon nanofiber (N-CNF) aerogels [134]. As Figure 1.15 showed that lyophilized bacterial cellulose was direct pyrolyzed to fabricate the N-CNF [134]. The ORR half-wave potential of the obtained N-CNF was only 50 mV lower than that of the Pt/C. Furthermore, when applying the N-CNF in ZABs, the N-CNF showed remarkable performance which had a high specific capacity (615 mAh g$^{-1}$) and energy density of 760 Wh kg$^{-1}$.

Gengfeng Zheng and coworkers used a high-throughput spray-drying technique to synthesize multiple elements (Fe, P, and N) co-doped carbon microspheres with a mesopore dominated (egg-carbon microspheres [CMS]) derived from eggs without the extrinsic doping sources (Figure 1.16a) [135]. They first mixed tetraethyl orthosilicate (TEOS) with eggs and spray-dried and then etched to obtain mesoporous structures. It was worth noting that the resulting co-doped egg-CMS having a high pore volume and a large specific surface area exhibited comparable catalytic activities for ORR. In addition, when used egg-CMS electrocatalyst as the air cathode in ZABs, it showed that the battery discharge voltage can be well maintained at about 1 V after 30 cycles. Orlando J. Rojas and coworkers used coconut shell residues to prepare N, P-doped porous carbon applying to the ORR in alkaline solution (Figure 1.16b) [136].

## 1.6 Conclusion

In summary, we reviewed the latest advance in the research of Pt-based materials, transition metals/alloys, transition metal oxides/sulfide, atomically dispersed metal in carbon materials, and metal-free carbon materials as ORR electrocatalysts, especially the mechanistic understanding of these catalysts and their performance in the air cathode discharge process of ZABs. To increase the active site of the metal-based catalysts under a limited mass loading, the catalyst size is typically reduced to the nanoscale. For metal-free carbon materials, to increase the exposure of the active sites and promote the diffusion of reactants and oxygen, hierarchical porosities are required. In general, dopants and structure internal defects can effectively increase the catalytic activity by modifying the electronic structure. At present, composite catalysts are composed of metal, alloys, metal oxides, metal sulfide, atomically dispersed metal in carbon, and metal-free carbon materials, such as heteroatom-doped carbon and defective carbon, exhibit promising properties due to their synergistic effects. Although many advances have been made in the ORR electrocatalysts for PEMFCs and ZABs, there are still challenges that require further development. For example, modifying metal-based NPs with organic or inorganic materials and supporting metals on robust support can optimize the surface electronic structure of the metal to increase the activity of the catalyst and stability, which provides a practical direction for preservation of the structural integrity of metal-based electrocatalyst in the future. Moreover, the metal-free catalysts have an effective catalytic ORR in alkaline electrolyte, but low activity and poor durability in acidic. Therefore, more research works on optimizing the synthesis conditions of the catalysts to achieve high catalytic activity and efficient use of active sites, thus improving ORR performance in both acidic and alkaline media.

## References

**1** Wu, K., Zhang, L., Yuan, Y. et al. (2020). An iron-decorated carbon aerogel for rechargeable flow and flexible Zn–air batteries. *Adv. Mater.* 32 (32): 2002292.

**2** Peng, X., Zhang, L., Chen, Z. et al. (2019). Hierarchically porous carbon plates derived from wood as bifunctional ORR/OER electrodes. *Adv. Mater.* 31 (16): 1900341.

**3** Xu, X., Song, F., and Hu, X. (2016). A nickel iron diselenide-derived efficient oxygen-evolution catalyst. *Nat. Nanotechnol.* 7: 12324.

**4** Wang, Z.-L., Xu, D., Xu, J.-J., and Zhang, X.-B. (2014). Oxygen electrocatalysts in metal–air batteries: from aqueous to nonaqueous electrolytes. *Chem. Soc. Rev.* 43 (22): 7746.

**5** Choi, S.I., Xie, S., Shao, M. et al. (2013). Synthesis and characterization of 9 nm Pt–Ni octahedra with a record high activity of 3.3 A/mg(Pt) for the oxygen reduction reaction. *Nano Lett.* 13 (7): 3420.

**6** Li, T., Chen, Y., Tang, Z. et al. (2019). Palladium nanoparticles supported by metal–organic frameworks derived $FeNi_3C_x$ nanorods as efficient oxygen reversible catalysts for rechargeable Zn–air batteries. *Electrochem. Acta* 307: 403.

**7** Nørskov, J.K., Rossmeisl, J., Logadottir, A. et al. (2004). Origin of the overpotential for oxygen reduction at a fuel-cell cathode. *J. Phys. Chem. B* 108 (46): 17886.

**8** Fu, J., Cano, Z.P., Park, M.G. et al. (2017). Electrically rechargeable zinc–air batteries: progress, challenges, and perspectives. *Adv. Mater.* 29 (7): 1604685.

**9** Meng, F., Zhong, H., Bao, D. et al. (2016). In situ coupling of strung $Co_4N$ and intertwined N-C fibers toward free-standing bifunctional cathode for robust, efficient, and flexible Zn–air batteries. *J. Am. Chem. Soc.* 138 (32): 10226.

**10** Li, J., Chen, M., Cullen, D.A. et al. (2018). Atomically dispersed manganese catalysts for oxygen reduction in proton-exchange membrane fuel cells. *Nat. Catal.* 1 (12): 935.

**11** Swette, L., Kackley, N., and McCatty, S. (1991). Oxygen electrodes for rechargeable alkaline fuel cells. *J. Power Sources* 36 (3): 323.

**12** Li, D., Wang, C., Strmcnik, D.S. et al. (2014). Functional links between Pt single crystal morphology and nanoparticles with different size and shape: the oxygen reduction reaction case. *Energy Environ. Sci.* 7 (12): 4061.

**13** Yan, D., Li, Y., Huo, J. et al. (2017). Defect chemistry of nonprecious-metal electrocatalysts for oxygen reactions. *Adv. Mater.* 29 (48): 1606459.

**14** Chao, W., Chi, M., Li, D. et al. (2011). Synthesis of homogeneous Pt-bimetallic nanoparticles as highly efficient electrocatalysts. *ACS Catal.* 1 (10): 1355.

**15** Stamenković, V.R., Fowler, B., Mun, B.S. et al. (2007). Improved oxygen reduction activity on $Pt_3Ni(111)$ via increased surface site availability. *Science* 315 (5811): 493.

**16** Mainar, A.R., Colmenares, L.C., Leonet, O. et al. (2016). Manganese oxide catalysts for secondary zinc air batteries: from electrocatalytic activity to bifunctional air electrode performance. *Electrochim. Acta* 217: 80.

**17** Zhang, J., Zhao, Z., Xia, Z., and Dai, L. (2015). A metal-free bifunctional electrocatalyst for oxygen reduction and oxygen evolution reactions. *Nat. Nanotechnol.* 10 (5): 444.

**18** Zhang, J., Xia, Z., and Dai, L. (2015). Carbon-based electrocatalysts for advanced energy conversion and storage. *Sci. Adv.* 1 (7): e1500564.

**19** Paul, R., Dai, Q., Hu, C., and Dai, L. (2019). Ten years of carbon-based metal-free electrocatalysts. *Carbon Energy* 1 (1): 19.

**20** Li, T., Yang, F., Cheng, G., and Luo, W. (2018). Reduced graphene oxide-wrapped $Co_{9-x}Fe_xS_8$/Co, Fe-N-C composite as bifunctional electrocatalyst for oxygen reduction and evolution. *Small* 14 (10): 1703748.

**21** Higgins, D., Hoque, M.A., Seo, M.H. et al. (2014). Development and simulation of sulfur-doped graphene supported platinum with exemplary stability and activity towards oxygen reduction. *Adv. Funct. Mater.* 24 (27): 4325.

**22** Tiwari, J.N., Nath, K., Kumar, S. et al. (2013). Stable platinum nanoclusters on genomic DNA-graphene oxide with a high oxygen reduction reaction activity. *Nat. Commun.* 4: 2221.

**23** Li, Y., Li, Y., Zhu, E. et al. (2012). Stabilization of high-performance oxygen reduction reaction Pt electrocatalyst supported on reduced graphene oxide/carbon black composite. *J. Am. Chem. Soc.* 134 (30): 12326.

**24** Nesselberger, M., Roefzaad, M., Hamou, R.F. et al. (2013). The effect of particle proximity on the oxygen reduction rate of size-selected platinum clusters. *Nat. Mater.* 12 (10): 919.

**25** Tripković, V., Cerri, I., Bligaard, T., and Rossmeisl, J. (2014). The influence of particle shape and size on the activity of platinum nanoparticles for oxygen reduction reaction: a density functional theory study. *Catal. Lett.* 144 (3): 380.

**26** Stephens, I.E., Bondarenko, A.S., Grønbjerg, U. et al. (2012). Understanding the electrocatalysis of oxygen reduction on platinum and its alloys. *Energy Environ. Sci.* 5 (5): 6744.

**27** Wang, C., Marković, N.M., and Stamenković, V.R. (2012). Advanced platinum alloy electrocatalysts for the oxygen reduction reaction. *ACS Catal.* 2 (5): 891.

**28** Sun, S.-G., Chen, A.-C., Huang, T.-S. et al. (1992). Electrocatalytic properties of Pt(111), Pt(332), Pt(331) and Pt(110) single crystal electrodes towards ethylene glycol oxidation in sulphuric acid solutions. *J. Electroanal. Chem.* 340 (1, 2): 213.

**29** Somorjai, G.A. and Blakely, D. (1975). Mechanism of catalysis of hydrocarbon reactions by platinum surfaces. *Nature* 258 (5536): 580.

**30** Tian, N., Zhou, Z.-Y., Sun, S.-G. et al. (2007). Synthesis of tetrahexahedral platinum nanocrystals with high-index facets and high electro-oxidation activity. *Science* 316 (5825): 732.

**31** Sheng, T., Xu, Y.-F., Jiang, Y.-X. et al. (2016). Structure design and performance tuning of nanomaterials for electrochemical energy conversion and storage. *Acc. Chem. Res.* 49 (11): 2569.

**32** Zhang, L., Roling, L.T., Wang, X. et al. (2015). Platinum-based nanocages with subnanometer-thick walls and well-defined, controllable facets. *Science* 349 (6246): 412.

**33** Koenigsmann, C., Zhou, W.-p., Adzic, R.R. et al. (2010). Size-dependent enhancement of electrocatalytic performance in relatively defect-free, processed ultrathin platinum nanowires. *Nano Lett.* 10 (8): 2806.

**34** Liang, H.W., Cao, X., Zhou, F. et al. (2011). A free-standing Pt-nanowire membrane as a highly stable electrocatalyst for the oxygen reduction reaction. *Adv. Mater.* 23 (12): 1467.

**35** Sun, S., Yang, D., Villers, D. et al. (2008). Template-and surfactant-free room temperature synthesis of self-assembled 3D Pt nanoflowers from single-crystal nanowires. *Adv. Mater.* 20 (3): 571.

**36** Xia, B.Y., Ng, W.T., Wu, H.B. et al. (2012). Self-supported interconnected Pt nanoassemblies as highly stable electrocatalysts for low-temperature fuel cells. *Angew. Chem. Int. Ed.* 51 (29): 7213.

**37** Greeley, J., Stephens, I.E.L., Bondarenko, A.S. et al. (2009). Alloys of platinum and early transition metals as oxygen reduction electrocatalysts. *Nat. Chem.* 1: 552.

**38** Park, J., Zhang, L., Choi, S.-I. et al. (2015). Atomic layer-by-layer deposition of platinum on palladium octahedra for enhanced catalysts toward the oxygen reduction reaction. *ACS Nano* 9 (3): 2635.

**39** Zhao, X., Chen, S., Fang, Z. et al. (2015). Octahedral Pd@$Pt_{1.8}$Ni core–shell nanocrystals with ultrathin PtNi alloy shells as active catalysts for oxygen reduction reaction. *J. Am. Chem. Soc.* 137 (8): 2804.

**40** Zhao, Z., Feng, M., Zhou, J. et al. (2016). Composition tunable ternary Pt-Ni-Co octahedra for optimized oxygen reduction activity. *Chem. Commun.* 52 (75): 11215.

**41** Kitchin, J.R., Nørskov, J.K., Barteau, M.A., and Chen, J.G. (2004). Role of strain and ligand effects in the modification of the electronic and chemical properties of bimetallic surfaces. *Phys. Rev. Lett.* 93 (15): 156801.

**42** Wu, J., Qi, L., You, H. et al. (2012). Icosahedral platinum alloy nanocrystals with enhanced electrocatalytic activities. *J. Am. Chem. Soc.* 134 (29): 11880.

**43** Strasser, P., Koh, S., Anniyev, T. et al. (2010). Lattice-strain control of the activity in dealloyed core–shell fuel cell catalysts. *Nat. Chem.* 2: 454.

**44** Stamenković, V., Schmidt, T.J., Ross, P.N., and Marković, N.M. (2002). Surface composition effects in electrocatalysis: kinetics of oxygen reduction on well-defined $Pt_3$Ni and $Pt_3$Co alloy surfaces. *J. Phys. Chem. B* 106 (46): 11970.

**45** Stamenković, V., Mun, B.S., Mayrhofer, K.J.J. et al. (2006). Changing the activity of electrocatalysts for oxygen reduction by tuning the surface electronic structure. *Angew. Chem. Int. Ed.* 45 (18): 2897.

**46** Stamenković, V.R., Mun, B.S., Arenz, M. et al. (2007). Trends in electrocatalysis on extended and nanoscale Pt-bimetallic alloy surfaces. *Nat. Mater.* 6 (3): 241.

**47** Yu, Y., Yang, W., Sun, X. et al. (2014). Monodisperse MPt (M = Fe, Co, Ni, Cu, Zn) nanoparticles prepared from a facile oleylamine reduction of metal salts. *Nano Lett.* 14 (5): 2778.

**48** Chen, C., Kang, Y., Huo, Z. et al. (2014). Highly crystalline multimetallic nanoframes with three-dimensional electrocatalytic surfaces. *Science* 343 (26): 1339.

**49** Wang, D., Xin, H.L., Hovden, R. et al. (2013). Structurally ordered intermetallic platinum–cobalt core–shell nanoparticles with enhanced activity and stability as oxygen reduction electrocatalysts. *Nat. Mater.* 12 (1): 81.

**50** Wang, D., Yu, Y., Xin, H.L. et al. (2012). Tuning oxygen reduction reaction activity via controllable dealloying: a model study of ordered $Cu_3Pt/C$ intermetallic nanocatalysts. *Nano Lett.* 12 (10): 5230.

**51** Wang, R., Xu, C., Bi, X., and Ding, Y. (2012). Nanoporous surface alloys as highly active and durable oxygen reduction reaction electrocatalysts. *Energy Environ. Sci.* 5 (1): 5281.

**52** Shui, J.L., Chen, C., and Li, J.C.M. (2011). Evolution of nanoporous Pt–Fe alloy nanowires by dealloying and their catalytic property for oxygen reduction reaction. *Adv. Funct. Mater.* 21 (17): 3357.

**53** Snyder, J., Mccue, I., Livi, K., and Erlebacher, J. (2012). Structure/processing/properties relationships in nanoporous nanoparticles as applied to catalysis of the cathodic oxygen reduction reaction. *J. Am. Chem. Soc.* 134 (20): 8633.

**54** Wang, D., Zhao, P., and Li, Y. (2011). General preparation for Pt-based alloy nanoporous nanoparticles as potential nanocatalysts. *Sci. Rep.* 1 (7): 37.

**55** Gan, L., Heggen, M., O’Malley, R. et al. (2013). Understanding and controlling nanoporosity formation for improving the stability of bimetallic fuel cell catalysts. *Nano Lett.* 13 (3): 1131.

**56** Meier, J.C., Galeano, C., Katsounaros, I. et al. (2012). Degradation mechanisms of Pt/C fuel cell catalysts under simulated start–stop conditions. *ACS Catal.* 2 (5): 832.

**57** Hartnig, C. and Schmidt, T.J. (2011). Simulated start-stop as a rapid aging tool for polymer electrolyte fuel cell electrodes. *J. Power Sources* 196 (13): 5564.

**58** Schmidt, T.J. and Baurmeister, J. (2008). Properties of high-temperature PEFC Celtec®-P 1000 MEAs in start/stop operation mode. *J. Power Sources* 176 (2): 428.

**59** Donthu, S., Cai, M., Ruthkosky, M., and Halalay, I. (2009). Carbon-titania composite substrates for fuel cell catalyst applications. *Chem. Commun.* 28 (28): 4203.

**60** Ying, L. and Mustain, W.E. (2011). Structural and electrochemical studies of Pt clusters supported on high-surface-area tungsten carbide for oxygen reduction. *ACS Catal.* 1 (3): 212.

**61** Yu, X. and Ye, S. (2007). Recent advances in activity and durability enhancement of Pt/C catalytic cathode in PEMFC: Part I. Physico-chemical and electronic interaction between Pt and carbon support, and activity enhancement of Pt/C catalyst. *J. Power Sources* 172 (1): 133.

**62** Cuong, N.T., Chi, D.H., Kim, Y.T., and Mitani, T. (2010). Structural and electronic properties of Pt-*n* ($n = 3, 7, 13$) clusters on metallic single wall carbon nanotube. *Phys. Status Solidi B* 243 (13): 3472.

**63** Fang, B., Kim, J.H., Kim, M., and Yu, J.S. (2009). Ordered hierarchical nanostructured carbon as a highly efficient cathode catalyst support in proton exchange membrane fuel cell. *Chem. Mater.* 21 (5): 789.

**64** Gupta, G., Slanac, D.A., Kumar, P. et al. (2010). Highly stable Pt/ordered graphitic mesoporous carbon electrocatalysts for oxygen reduction. *J. Phys. Chem. C* 114 (24): 10796.

**65** Carolina, G., Meier, J.C., Volker, P. et al. (2012). Toward highly stable electrocatalysts via nanoparticle pore confinement. *J. Am. Chem. Soc.* 134 (50): 20457.

**66** Liu, Y., Shrestha, S., and Mustain, W.E. (2012). Synthesis of nanosize tungsten oxide and its evaluation as an electrocatalyst support for oxygen reduction in acid media. *ACS Catal.* 2 (3): 456.

**67** Huang, S.Y., Ganesan, P., and Popov, B.N. (2012). Electrocatalytic activity and stability of titania-supported platinum-palladium electrocatalysts for polymer electrolyte membrane fuel cell. *ACS Catal.* 2 (2): 825.

**68** Yao, C., Li, F., Li, X., and Xia, D. (2012). Fiber-like nanostructured $Ti_4O_7$ used as durable fuel cell catalyst support in oxygen reduction catalysis. *J. Mater. Chem.* 22 (32): 16560.

**69** Liu, H.J., Wang, F., Zhao, Y., and Fong, H. (2013). Mechanically resilient electrospun TiC nanofibrous mats surface-decorated with Pt nanoparticles for oxygen reduction reaction with enhanced electrocatalytic activities. *Nanoscale* 5 (9): 3643.

**70** Liu, Y. and Mustain, W.E. (2013). High stability, high activity Pt/ITO oxygen reduction electrocatalysts. *J. Am. Chem. Soc.* 135 (2): 530.

**71** Ho, V.T.T., Pan, C.J., Rick, J. et al. (2011). Nanostructured $Ti_{0.7}Mo_{0.3}O_2$ support enhances electron transfer to Pt: high-performance catalyst for oxygen reduction reaction. *J. Am. Chem. Soc.* 133 (30): 11716.

**72** Xie, X., Xue, Y., Li, L. et al. (2014). Surface Al leached $Ti_3AlC_2$ as a substitute for carbon for use as a catalyst support in a harsh corrosive electrochemical system. *Nanoscale* 6 (19): 11035.

**73** Xie, X., Chen, S., Ding, W. et al. (2013). An extraordinarily stable catalyst: Pt NPs supported on two-dimensional $Ti_3C_2X_2$ ($X = OH, F$) nanosheets for oxygen reduction reaction. *Chem. Commun.* 49 (86): 10112.

**74** Wang, J., Wu, H., Gao, D. et al. (2015). High-density iron nanoparticles encapsulated within nitrogen-doped carbon nanoshell as efficient oxygen electrocatalyst for zinc–air battery. *Nano Energy* 13: 387.

**75** Yang, Z.K., Lin, L., and Xu, A.W. (2016). 2D Nanoporous Fe-N/C nanosheets as highly efficient non-platinum electrocatalysts for oxygen reduction reaction in Zn–air battery. *Small* 12 (41): 5710.

**76** Ahn, S.H., Yu, X., and Manthiram, A. (2017). “Wiring” Fe–$N_x$ embedded porous carbon framework onto 1D nanotubes for efficient oxygen reduction reaction in alkaline and acidic media. *Adv. Mater.* 29 (26): 1606534.

**77** Jin, H., Zhou, H., Li, W. et al. (2018). In situ derived Fe/N/S-codoped carbon nanotubes from ZIF-8 crystals as efficient electrocatalysts for the oxygen reduction reaction and zinc–air batteries. *J. Mater. Chem. A* 6 (41): 20093.

**78** Fu, K., Wang, Y., Mao, L. et al. (2018). Strongly coupled Co, N co-doped carbon nanotubes/graphene-like carbon nanosheets as efficient oxygen reduction electrocatalysts for primary zinc–air battery. *Chem. Eng. J.* 351: 94.

**79** Wu, H., Jiang, X., Ye, Y. et al. (2017). Nitrogen-doped carbon nanotube encapsulating cobalt nanoparticles towards efficient oxygen reduction for zinc–air battery. *J. Energy Chem.* 26 (6): 1181.

**80** Zhou, K.-Y., Chen, G.-Y., Liu, J.-A. et al. (2016). Cobalt nanoparticles encapsulated in N-doped graphene nanoshells as an efficient cathode electrocatalyst for a mechanical rechargeable zinc–air battery. *RSC Adv.* 6 (93): 90069.

**81** Jia, G., Zhang, W., Fan, G. et al. (2017). Three-dimensional hierarchical architectures derived from surface-mounted metal-organic framework membranes for enhanced electrocatalysis. *Angew. Chem. Int. Ed. Engl.* 56 (44): 13781.

**82** Su, Y., Zhu, Y., Jiang, H. et al. (2014). Cobalt nanoparticles embedded in N-doped carbon as an efficient bifunctional electrocatalyst for oxygen reduction and evolution reactions. *Nanoscale* 6 (24): 15080.

**83** Liu, S., Wang, Z., Zhou, S. et al. (2017). Metal–organic-framework-derived hybrid carbon nanocages as a bifunctional electrocatalyst for oxygen reduction and evolution. *Adv. Mater.* 29 (31): 1700874.

**84** Su, C.-Y., Cheng, H., Li, W. et al. (2017). Atomic modulation of FeCo–nitrogen–carbon bifunctional oxygen electrodes for rechargeable and flexible all-solid-state zinc–air battery. *Adv. Energy Mater.* 7 (13): 1602420.

**85** Wang, T., Kou, Z., Mu, S. et al. (2018). 2D dual-metal zeolitic-imidazolate-framework-(ZIF)-derived bifunctional air electrodes with ultrahigh electrochemical properties for rechargeable zinc–air batteries. *Adv. Funct. Mater.* 28 (5): 1705048.

**86** Zhu, J., Xiao, M., Zhang, Y. et al. (2016). Metal–organic framework-induced synthesis of ultrasmall encased NiFe nanoparticles coupling with graphene as an efficient oxygen electrode for a rechargeable Zn–air battery. *ACS Catal.* 6 (10): 6335.

**87** Fu, G., Chen, Y., Cui, Z. et al. (2016). Novel hydrogel-derived bifunctional oxygen electrocatalyst for rechargeable air cathodes. *Nano Lett.* 16 (10): 6516.

**88** Chen, Z., Yu, A., Ahmed, R. et al. (2012). Manganese dioxide nanotube and nitrogen-doped carbon nanotube based composite bifunctional catalyst for rechargeable zinc–air battery. *Electrochim. Acta* 69: 295.

**89** Ding, J., Ji, S., Wang, H. et al. (2019). MnO/N-doped mesoporous carbon as advanced oxygen reduction reaction electrocatalyst for zinc–air batteries. *Chemistry* 25 (11): 2868.

**90** Liang, Y., Li, Y., Wang, H. et al. (2011). $Co_3O_4$ nanocrystals on graphene as a synergistic catalyst for oxygen reduction reaction. *Nat. Mater.* 10 (10): 780.

**91** Liang, Y., Wang, H., Zhou, J. et al. (2012). Covalent hybrid of spinel manganese–cobalt oxide and graphene as advanced oxygen reduction electrocatalysts. *J. Am. Chem. Soc.* 134 (7): 3517.

**92** Li, Y., Zhong, C., Liu, J. et al. (2018). Atomically thin mesoporous $Co_3O_4$ layers strongly coupled with N-rGO nanosheets as high-performance bifunctional catalysts for 1D knittable zinc–air batteries. *Adv. Mater.* 30 (4): 1703657.

**93** Hao, Y., Xu, Y., Han, N. et al. (2017). Boosting the bifunctional electrocatalytic oxygen activities of $CoO_x$ nanoarrays with a porous N-doped carbon coating and their application in Zn–air batteries. *J. Mater. Chem. A* 5 (34): 17804.

**94** Guan, C., Sumboja, A., Wu, H. et al. (2017). Hollow $Co_3O_4$ nanosphere embedded in carbon arrays for stable and flexible solid-state zinc–air batteries. *Adv. Mater.* 29 (44): 1704117.

**95** Zhou, T., Xu, W., Zhang, N. et al. (2019). Ultrathin cobalt oxide layers as electrocatalysts for high-performance flexible Zn–air batteries. *Adv. Mater.* 31 (15): e1807468.

**96** Hamdani, M., Singh, R., and Chartier, P. (2010). $Co_3O_4$ and Co-based spinel oxides bifunctional oxygen electrodes. *Int. J. Electrochem. Sci.* 5 (4): 556.

**97** Liu, W., Bao, J., Xu, L. et al. (2019). $NiCo_2O_4$ ultrathin nanosheets with oxygen vacancies as bifunctional electrocatalysts for Zn–air battery. *Appl. Surf. Sci.* 478: 552.

**98** Wei, L., Karahan, H.E., Zhai, S. et al. (2017). Amorphous bimetallic oxide-graphene hybrids as bifunctional oxygen electrocatalysts for rechargeable Zn–air batteries. *Adv. Mater.* 29 (38): 1701410.

**99** Jiang, S., Ithisuphalap, K., Zeng, X. et al. (2018). 3D porous cellular $NiCoO_2$/graphene network as a durable bifunctional electrocatalyst for oxygen evolution and reduction reactions. *J. Power Sources* 399: 66.

**100** Gao, M.-R., Xu, Y.-F., Jiang, J., and Yu, S.-H. (2013). Nanostructured metal chalcogenides: synthesis, modification, and applications in energy conversion and storage devices. *Chem. Soc. Rev.* 42 (7): 2986.

**101** Xia, W., Mahmood, A., Liang, Z. et al. (2016). Earth-abundant nanomaterials for oxygen reduction. *Angew. Chem. Int. Ed.* 55 (8): 2650.

**102** Indra, A., Menezes, P.W., Sahraie, N.R. et al. (2014). Unification of catalytic water oxidation and oxygen reduction reactions: amorphous beat crystalline cobalt iron oxides. *J. Am. Chem. Soc.* 136 (50): 17530.

**103** Wang, J., Li, L., Chen, X. et al. (2016). Monodisperse cobalt sulfides embedded within nitrogen-doped carbon nanoflakes: an efficient and stable electrocatalyst for the oxygen reduction reaction. *J. Mater. Chem. A* 4 (29): 11342.

**104** Guo, L., Deng, J., Wang, G. et al. (2018). N, P-doped $CoS_2$ embedded in $TiO_2$ nanoporous films for Zn-air batteries. *Adv. Funct. Mater.* 28 (42): 1804540.

**105** Fu, J., Hassan, F.M., Zhong, C. et al. (2017). Defect engineering of chalcogen-tailored oxygen electrocatalysts for rechargeable quasi-solid-state zinc–air batteries. *Adv. Mater.* 29 (35): 1702526.

**106** Tang, Y., Jing, F., Xu, Z. et al. (2017). Highly crumpled hybrids of nitrogen/sulfur dual-doped graphene and $Co_9S_8$ nanoplates as efficient bifunctional oxygen electrocatalysts. *ACS Appl. Mater. Interfaces* 9 (14): 12340.

**107** Li, Y., Zhou, W., Dong, J. et al. (2018). Interface engineered in situ anchoring of $Co_9S_8$ nanoparticles into a multiple doped carbon matrix: highly efficient zinc–air batteries. *Nanoscale* 10 (5): 2649.

**108** Zhang, Z., Wang, X., Cui, G. et al. (2014). $NiCo_2S_4$ sub-micron spheres: an efficient non-precious metal bifunctional electrocatalyst. *Nanoscale* 6 (7): 3540.

**109** Zhang, J., Bai, X., Wang, T. et al. (2019). Bimetallic nickel cobalt sulfide as efficient electrocatalyst for Zn–air battery and water splitting. *Nano-Micro. Lett.* 11 (1): 2.

**110** Han, X., Wu, X., Cheng, Z. et al. (2017). $NiCo_2S_4$ nanocrystals anchored on nitrogen-doped carbon nanotubes as a highly efficient bifunctional electrocatalyst for rechargeable zinc–air batteries. *Nano Energy* 31: 541.

**111** Liu, W., Zhang, J., Bai, Z. et al. (2018). Controllable urchin-like $NiCo_2S_4$ microsphere synergized with sulfur-doped graphene as bifunctional catalyst for superior rechargeable Zn–air battery. *Adv. Funct. Mater.* 28 (11): 1706675.

**112** Yang, X., Wang, A., Qiao, B. et al. (2013). Single-atom catalysts: a new frontier in heterogeneous catalysis. *Acc. Chem. Res.* 46 (8): 1740.

**113** Cordón, J., Jiménezosés, G., Lópezdeluzuriaga, J.M., and Monge, M. (2017). The key role of Au-substrate interactions in catalytic gold subnanoclusters. *Nat. Commun.* 8 (1): 1657.

**114** Zhang, L., Han, L., Liu, H. et al. (2017). Potential-cycling synthesis of single platinum atoms for efficient hydrogen evolution in neutral media. *Angew. Chem. Int. Ed.* 56 (44): 13694.

**115** Choi, C.H., Kim, M., Kwon, H.C. et al. (2016). Tuning selectivity of electrochemical reactions by atomically dispersed platinum catalyst. *Nat. Commun.* 7: 10922.

**116** Liu, J., Jiao, M., Lu, L. et al. (2017). High performance platinum single atom electrocatalyst for oxygen reduction reaction. *Nat. Commun.* 8: 15938.

**117** Zeng, X., Shui, J., Liu, X. et al. (2018). Single-atom to single-atom grafting of $Pt_1$ onto $Fe–N_4$ center: $Pt_1$@Fe-N-C multifunctional electrocatalyst with significantly enhanced properties. *Adv. Energy Mater.* 8 (1): 1701345.

**118** Tang, C., Wang, B., Wang, H.F., and Zhang, Q. (2017). Defect engineering toward atomic $Co–N_x–C$ in hierarchical graphene for rechargeable flexible solid Zn–air batteries. *Adv. Mater.* 29 (37): 1703185.

**119** Ma, L., Chen, S., Pei, Z. et al. (2018). Single-site active iron-based bifunctional oxygen catalyst for a compressible and rechargeable zinc–air battery. *ACS Nano* 12 (2): 1949.

**120** Han, Y., Wang, Y.G., Chen, W. et al. (2017). Hollow N-doped carbon spheres with isolated cobalt single atomic sites: superior electrocatalysts for oxygen reduction. *J. Am. Chem. Soc.* 139 (48): 17269.

**121** Li, Q., Chen, W., Xiao, H. et al. (2018). Fe isolated single atoms on S, N codoped carbon by copolymer pyrolysis strategy for highly efficient oxygen reduction reaction. *Adv. Mater.* 30 (25): e1800588.

**122** Yin, P., Yao, T., Wu, Y. et al. (2016). Single cobalt atoms with precise N-coordination as superior oxygen reduction reaction catalysts. *Angew. Chem. Int. Ed.* 55 (36): 10800.

**123** Zhao, L., Zhang, Y., Huang, L.-B. et al. (2019). Cascade anchoring strategy for general mass production of high-loading single-atomic metal–nitrogen catalysts. *Nat. Commun.* 10 (1): 1278.

**124** Chen, Y., Ji, S., Wang, Y. et al. (2017). Isolated single iron atoms anchored on N-doped porous carbon as an efficient electrocatalyst for the oxygen reduction reaction. *Angew. Chem. Int. Ed.* 56 (24): 6937.

**125** Ma, Z., Dou, S., Shen, A. et al. (2015). Sulfur-doped graphene derived from cycled lithium–sulfur batteries as a metal-free electrocatalyst for the oxygen reduction reaction. *Angew. Chem. Int. Ed.* 54 (6): 1888.

**126** Zehtab Yazdi, A., Fei, H., Ye, R. et al. (2015). Boron/nitrogen co-doped helically unzipped multiwalled carbon nanotubes as efficient electrocatalyst for oxygen reduction. *ACS Appl. Mater. Interfaces* 7 (14): 7786.

**127** Jeon, I.Y., Zhang, S., Zhang, L. et al. (2013). Edge-selectively sulfurized graphene nanoplatelets as efficient metal-free electrocatalysts for oxygen reduction reaction: the electron spin effect. *Adv. Mater.* 25 (42): 6138.

**128** Gong, Y., Fei, H., Zou, X. et al. (2015). Boron- and nitrogen-substituted graphene nanoribbons as efficient catalysts for oxygen reduction reaction. *Chem. Mater.* 27 (4): 1181.

**129** Su, Y., Yao, Z., Zhang, F. et al. (2016). Sulfur-enriched conjugated polymer nanosheet derived sulfur and nitrogen co-doped porous carbon nanosheets as electrocatalysts for oxygen reduction reaction and zinc–air battery. *Adv. Funct. Mater.* 26 (32): 5893.

**130** Wang, J., Hao, J., Liu, D. et al. (2017). Porous boron carbon nitride nanosheets as efficient metal-free catalysts for the oxygen reduction reaction in both alkaline and acidic solutions. *ACS Energy Lett.* 2 (2): 306.

**131** Wei, W., Liang, H., Parvez, K. et al. (2014). Nitrogen-doped carbon nanosheets with size-defined mesopores as highly efficient metal-free catalyst for the oxygen reduction reaction. *Angew. Chem. Int. Ed.* 53 (6): 1570.

**132** Graglia, M., Pampel, J., Hantke, T. et al. (2016). Nitro lignin-derived nitrogen-doped carbon as an efficient and sustainable electrocatalyst for oxygen reduction. *ACS Nano* 10 (4): 4364.

**133** Zhang, J., Zhang, C., Zhao, Y. et al. (2017). Three dimensional few-layer porous carbon nanosheets towards oxygen reduction. *Appl. Catal., B* 211: 148.

**134** Liang, H.W., Wu, Z.Y., Chen, L.F. et al. (2015). Bacterial cellulose derived nitrogen-doped carbon nanofiber aerogel: an efficient metal-free oxygen reduction electrocatalyst for zinc–air battery. *Nano Energy* 11: 366.

**135** Wu, H., Geng, J., Ge, H. et al. (2016). Egg-derived mesoporous carbon microspheres as bifunctional oxygen evolution and oxygen reduction electrocatalysts. *Adv. Energy Mater.* 6 (20): 1600794.

**136** Borghei, M., Laocharoen, N., Kibena-Põldsepp, E. et al. (2017). Porous N, P-doped carbon from coconut shells with high electrocatalytic activity for oxygen reduction: alternative to Pt–C for alkaline fuel cells. *Appl. Catal., B* 204: 394.